ICTP Physics Without Frontiers (PWF)

Physics for Bangladesh – Online Summer Internship

Internship Report

Numerical analysis of inflationary α-attractor models

Masuk Ridwan Saumo

BSc. in Electrical and Electronic Engineering
Bangladesh University of Engineering and Technology

Supervisor:
Rafid Mahbub, Ph.D.
DataKind

Internship Period:
15 July 2025 – 15 October 2025

November 26, 2025
International Centre for Theoretical Physics (ICTP)

Abstract

We study the inflationary dynamics of α-attractor models, focusing on both E- and T-model potentials. These models provide a unified framework encompassing a wide class of inflationary scenarios whose predictions converge toward the quadratic and Starobinsky limits. The background dynamics are investigated by numerically solving the Klein–Gordon and Friedmann equations under suitable dimensionless parametrizations. We then analyze the evolution of the Hubble slow-roll parameters, e-fold number, and related inflationary observables such as the scalar spectral index n_s and tensor-to-scalar ratio r. These are required to be consistent with observational constraints. Furthermore, we numerically integrate the Mukhanov–Sasaki equations for scalar and tensor perturbations to obtain the primordial power spectra and compare them with slow-roll approximations. For the E-model, we examine the Starobinsky potential ($n = 1$, $\lambda_E = \sqrt{2/3}$) and its generalizations for $n = 2, 3$. For the T-model, we explore both the quadratic limit ($n = 1$, $\lambda_T = 10^{-4}$) and the effect of varying n with constant $\lambda_T = 0.5$. The resulting predictions for (n_s, r) are compared with the latest Planck 2018 [1] and BICEP/Keck [2] constraints, showing excellent agreement within observational bounds.

Contents

Chapter 1

Introduction

Cosmic inflation, a phase of accelerated expansion in the early Universe, provides a compelling solution to the horizon, flatness, and monopole problems of the standard Big Bang cosmology [3, 4, 5]. Moreover, quantum fluctuations of the inflaton field during inflation generate nearly scale-invariant primordial perturbations, which later evolve into the large-scale structure observed in the Universe today. Precise measurements of the Cosmic Microwave Background (CMB) anisotropies by missions such as *Planck* [1] and BICEP/Keck [2] have placed stringent constraints on inflationary models through observables like the scalar spectral index n_s and tensor-to-scalar ratio r.

Among the various theoretical frameworks proposed to describe inflation, the class of α-attractor models [6, 7] has attracted significant attention for its universality and predictive power. These models are characterized by potentials that depend on a single parameter α, which controls the curvature of the scalar field manifold. In the limit $\alpha \to 1$, they reproduce the predictions of the Starobinsky R^2 model [8], while for larger α values, they interpolate toward chaotic-type polynomial potentials. Two important subclasses of α-attractors are the E-models and T-models, which differ in their functional forms.

In this work, we carry out a detailed numerical study of both E- and T-models. We first analyze the background dynamics by solving the Friedmann and Klein–Gordon equations in dimensionless form using `scipy.integrate.solve_ivp`. This allows us to track the evolution of the inflaton field ϕ, its derivative $\dot{\phi}$, and the Hubble parameter H throughout the inflationary epoch. We compute the number of e-folds N, Hubble slow-roll parameters (ϵ_H, η_H), and key observables such as (n_s, r) under the slow-roll approximation.

For the E-model potential, we investigate the canonical Starobinsky case with $(n = 1, \lambda_E = \sqrt{2/3})$ and compare it with the generalized cases $n = 2$ and $n = 3$.

Similarly, for the T-model potential, we explore two scenarios: the quadratic limit with $(n = 1, \lambda_T = 10^{-4})$, and the variation of n for a fixed coupling $\lambda_T = 0.5$.

We further solve the Mukhanov–Sasaki equations for both scalar and tensor perturbations to obtain the full numerical power spectra beyond the slow-roll approximation. The scalar and tensor amplitudes $(\mathcal{P}_\zeta, \mathcal{P}_T)$ and spectral indices (n_s, n_T) are computed and compared with analytical slow-roll results. The numerically derived spectra are then compared with the latest observational constraints arising from Planck 2018 and BICEP/Keck.

This report is structured as follows: Section 2 describes the theoretical framework and motivation behind inflation as a cosmological theory. Section 3 presents the formulation of inflation, how it solves the problems of big-bang cosmology and different types of preliminary inflationary scenarios. Section 4 discusses the results for the E- and T-model potentials, including comparisons with different n-valued potentials. Finally, Section 5 summarizes the findings and outlines potential directions for future work.

In this report, we work with the natural system of units where $c = \hbar = k_\mathrm{B} = 1$ and use the mostly negative signature for the metric tensor $(+, -, -, -)$. We also define *reduced Planck mass* as $m_p = 1/\sqrt{8\pi G}$.

Chapter 2

Theoretical Background

2.1 Friedmann-Robertson-Walker (FRW) Metric

On large scales (~ 100Mpc), the observable Universe appears to be *homogeneous* and *isotropic*. The most general line element consistent with these symmetries can be written as [9, 10, 11]:

$$ds^2 = dt^2 - a(t)^2 \left[\frac{dr^2}{1 - kr^2} + r^2 (d\theta^2 + \sin^2 \theta \, d\phi^2) \right], \tag{2.1}$$

where $a(t)$ is the scale factor and k determines the spatial curvature:

$$k = \begin{cases} +1 & \text{closed (spherical) geometry,} \\ 0 & \text{flat geometry,} \\ -1 & \text{open (hyperbolic) geometry.} \end{cases}$$

It is convenient to express the metric in an alternative form [12],

$$ds^2 = dt^2 - a(t)^2 \left[d\chi^2 + S_k^2(\chi) \, (d\theta^2 + \sin^2 \theta \, d\phi^2) \right], \tag{2.2}$$

where the function $S_k(\chi)$ plays the role of a generalized radius and is defined as

$$S_k(\chi) = \begin{cases} \sin \chi, & k = +1, \\ \chi, & k = 0, \\ \sinh \chi, & k = -1. \end{cases}$$

2.2 Hubble Parameter

The Friedmann–Robertson–Walker (FRW) metric is not invariant under Lorentz transformations. Consequently, the Universe defines a *preferred rest frame*, described by the co-moving coordinates [11]. Although we can still perform spatial translations (in the flat case) and rotations, Lorentz boosts are no longer symmetries of the spacetime.

Consider a galaxy following a trajectory $\mathbf{x}(t)$ in co-moving coordinates. Its position in *physical coordinates* is given by

$$\mathbf{x}_{\rm phys}(t) = a(t)\,\mathbf{x}(t), \tag{2.3}$$

where $a(t)$ is the scale factor. Differentiating with respect to time, we obtain the *physical velocity*:

$$\mathbf{v}_{\rm phys}(t) = \frac{d\mathbf{x}_{\rm phys}}{dt} = \dot{a}(t)\,\mathbf{x}(t) + a(t)\,\frac{d\mathbf{x}}{dt} = H(t)\,\mathbf{x}_{\rm phys} + \mathbf{v}_{\rm pec}, \tag{2.4}$$

where the first term, $H(t)\,\mathbf{x}_{\rm phys}$, arises purely from the cosmic expansion and involves the *Hubble parameter*,

$$H(t) = \frac{\dot{a}(t)}{a(t)}. \tag{2.5}$$

The second term, $\mathbf{v}_{\rm pec}$, represents the *peculiar velocity* — the motion of the galaxy relative to the cosmological rest frame, typically caused by the gravitational influence of nearby structures.

Our own peculiar velocity is approximately $v_{\rm pec} \simeq 400\ \mathrm{km\,s^{-1}}$, which is typical for a galaxy [12]. The present-day value of the Hubble parameter, often called the *Hubble constant*, is

$$H_0 \simeq 70\ \mathrm{km\,s^{-1}\,Mpc^{-1}}. \tag{2.6}$$

The Hubble parameter has dimensions of inverse time, but it is conventionally written in the somewhat unusual units of $\mathrm{km\,s^{-1}\,Mpc^{-1}}$. This indicates that a galaxy located $1\ \mathrm{Mpc}$ away will appear to recede at a velocity of $70\ \mathrm{km\,s^{-1}}$ purely due to the cosmic expansion.

Neglecting peculiar velocities and assuming that $H(t)$ can be approximated as constant, $H(t) \approx H_0$, Eq. (2.4) reduces to the familiar linear relation

$$\mathbf{v}_{\rm phys} = H_0\,\mathbf{x}_{\rm phys}, \tag{2.7}$$

which is known as *Hubble's law* [9].

2.3 Cosmological Redshift

In a spacetime metric, light follows null geodesics characterized by $ds = 0$. For the Friedmann–Robertson–Walker (FRW) metric (Eq. 2.1), a radially traveling light ray (with fixed θ and ϕ) satisfies [10]

$$dt = \pm a(t)\,\frac{dr}{\sqrt{1-kr^2}}, \tag{2.8}$$

where the minus sign corresponds to light moving toward an observer at the origin, and the plus sign describes light moving away.

Consider a galaxy at a fixed comoving coordinate r_1 that emits a photon at cosmic time t_1. An observer at $r = 0$ receives this photon at time t_0, which is determined from

$$\int_{t_1}^{t_0} \frac{dt}{a(t)} = \int_0^{r_1} \frac{dr}{\sqrt{1-kr^2}}. \tag{2.9}$$

If the same galaxy emits another photon at a slightly later time $t_1 + \delta t_1$, it will be observed at $t_0 + \delta t_0$, satisfying

$$c\int_{t_1+\delta t_1}^{t_0+\delta t_0} \frac{dt}{a(t)} = \int_0^{r_1} \frac{dr}{\sqrt{1-kr^2/R^2}}. \tag{2.10}$$

Since the right-hand side depends only on the comoving coordinate, it is the same for both integrals. Subtracting the two equations yields

$$\frac{\delta t_1}{a(t_1)} = \frac{\delta t_0}{a(t_0)}. \tag{2.11}$$

Using the normalization $a(t_0) = 1$ for the present epoch, we obtain $\delta t_1/a(t_1) = \delta t_0$.

This shows that the time interval between successive emissions differs from that between their observations due to cosmic expansion. If the source emits two successive wave crests separated by $\delta t_1 = \lambda_1/c$, where λ_1 is the emitted wavelength, then the observer measures a time interval $\delta t_0 = \lambda_0/c$, where λ_0 is the observed wavelength. Equation (2.11) implies

$$\lambda_0 = \frac{a(t_0)}{a(t_1)}\lambda_1 = \frac{\lambda_1}{a(t_1)}, \tag{2.12}$$

indicating that light is stretched by the expansion of the universe as it propagates through space. This phenomenon is known as the *cosmological redshift* [11].

Although it resembles the Doppler effect, the two are distinct: the Doppler shift depends on relative velocity between source and observer, whereas cosmological redshift arises from the cumulative stretching of space, independent of $\dot{a}(t)$.

The redshift parameter z is defined as the fractional increase in observed wavelength:

$$z = \frac{\lambda_0 - \lambda_1}{\lambda_1} = \frac{1 - a(t_1)}{a(t_1)} \quad \Rightarrow \quad 1 + z = \frac{1}{a(t)}. \tag{2.13}$$

Hence, the present epoch corresponds to $z = 0$, while $z = 1$ and $z = 2$ correspond to epochs when the universe was half and one-third of its current size, respectively.

The redshift z is directly measurable: light from distant galaxies carries spectral absorption lines characteristic of the atomic and molecular composition of their stars. By comparing these spectral lines with their laboratory frequencies on Earth, one can infer the redshift and thus determine the scale factor at emission. Such measurements also confirm that the fundamental laws of physics and constants remain unchanged across cosmological distances and epochs [10].

2.4 Conformal Time & Null Geodesics

We now introduce the *conformal time* τ, defined through the differential relation [9, 12]

$$d\tau = \frac{dt}{a(t)}, \tag{2.14}$$

In terms of τ, the FRW metric takes the form

$$ds^2 = a^2(\tau) \left[d\tau^2 - d\chi^2 - S_k^2(\chi) \left(d\theta^2 + \sin^2\theta \, d\phi^2 \right) \right]. \tag{2.15}$$

This representation makes the causal structure of spacetime particularly transparent. For null geodesics ($ds^2 = 0$) in an isotropic universe, where θ and ϕ remain constant, we find [13]

$$\tau(\chi) = \pm\chi + \text{constant}. \tag{2.16}$$

Thus, light rays in conformal coordinates propagate along straight lines at 45°, just as in flat spacetime.

These null geodesics propagate at 45° in the (τ, χ) plane, exactly as they do in Minkowski spacetime. This happens because, apart from the angular part, the

metric in Eq. (2.15) is *conformally flat*: light travels as it would in Minkowski space when expressed in the conformal coordinates (τ, χ).

It is important to note that this simple causal behavior would not hold if we used the cosmic time t instead. In that case, t represents the proper time measured by comoving observers (i.e., observers at fixed spatial coordinates in the FRW slicing), and the metric is not manifestly conformally flat in those coordinates [10].

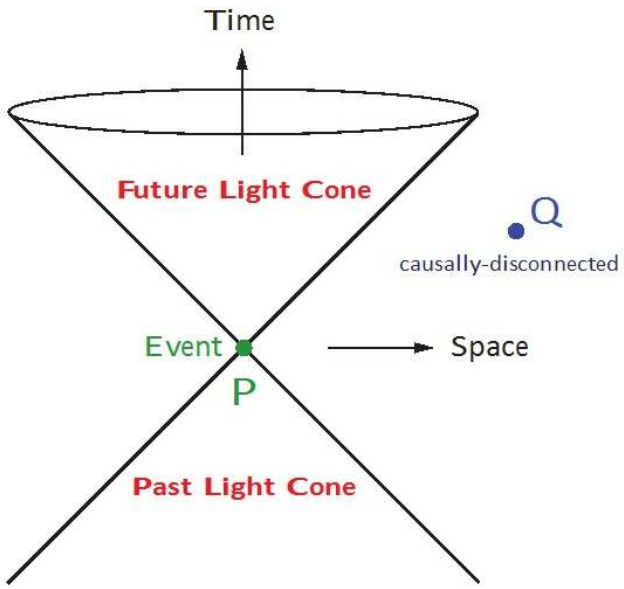

Figure 2.1: Propagation of signals in the $\tau - \chi$ plane. Photons move along null geodesics with zero proper time ($ds^2 = 0$), while massive particles follow timelike geodesics with real proper time ($ds^2 > 0$). Regions separated by spacelike intervals ($ds^2 < 0$) are causally disconnected. The collection of all null geodesics through a point forms its *light cone*. The interior of this cone, comprising timelike and null paths, defines the causally connected region of spacetime [13].

2.5 Continuity Equation

The stress–energy tensor for a perfect fluid can be expressed in an explicitly covariant form as

$$T^{\mu}_{\ \nu} = (\rho + P)U^{\mu}U_{\nu} - P\,\delta^{\mu}_{\ \nu}, \tag{2.17}$$

where $U^{\mu} \equiv dX^{\mu}/ds$ represents the four–velocity of the fluid relative to the observer, and ρ and P denote the energy density and pressure, respectively, measured in the rest frame of the fluid [9].

In Minkowski space, the conservation of energy and momentum implies the covariant conservation law

$$\nabla_\mu T^\mu_{\ \nu} = \partial_\mu T^\mu_{\ \nu} + \Gamma^\mu_{\ \mu\lambda} T^\lambda_{\ \nu} - \Gamma^\lambda_{\ \mu\nu} T^\mu_{\ \lambda} = 0, \tag{2.18}$$

which corresponds to four independent equations, one for each value of ν [14]. The time component is obtained by setting $\nu = 0$, leading to

$$\partial_\mu T^\mu_{\ 0} + \Gamma^\mu_{\ \mu\lambda} T^\lambda_{\ 0} - \Gamma^\lambda_{\ \mu 0} T^\mu_{\ \lambda} = 0. \tag{2.19}$$

Due to isotropy, $T^i_{\ 0} = 0$, so the equation simplifies to

$$\frac{d\rho}{dt} + \Gamma^\mu_{\ \mu 0}\rho - \Gamma^\lambda_{\ \mu 0} T^\mu_{\ \lambda} = 0. \tag{2.20}$$

From Eq. (1.2.41), the Christoffel symbols $\Gamma^\lambda_{\ \mu 0}$ vanish unless both λ and μ are spatial indices and equal, in which case $\Gamma^i_{\ i0} = \dot{a}/a$. Substituting this into Eq. (2.20) yields the continuity equation [9, 12],

$$\dot{\rho} + 3\frac{\dot{a}}{a}(\rho + P) = 0, \tag{2.21}$$

which describes the evolution of the energy density of the cosmic fluid in an expanding universe. If we specify a linear equation of state of the form,

$$P = w\,\rho, \tag{2.22}$$

the continuity equation (2.21) can be integrated to determine how the energy density evolves with the scale factor $a(t)$. We find

$$\frac{\dot{\rho}}{\rho} = -3(1+w)\frac{\dot{a}}{a} \tag{2.23}$$

$$\Rightarrow \log\frac{\rho}{\rho_0} = -3(1+w)\log a \tag{2.24}$$

$$\Rightarrow \rho(a) = \rho_0\, a^{-3(1+w)}, \tag{2.25}$$

where $\rho_0 = \rho(t_0)$ is the energy density at the present epoch, $a(t_0) = 1$ [9]. For *dust* (non-relativistic matter), $w = 0$, which gives

$$\rho_m \sim \frac{1}{a^3}. \tag{2.26}$$

For *radiation*, $w = 1/3$, yielding

$$\rho_r \sim \frac{1}{a^4}. \tag{2.27}$$

Here, in addition to the dilution by volume ($1/a^3$), there is an extra factor of $1/a$ due to the cosmological redshift [12].

Observations indicate that matter and radiation alone cannot account for the current evolution of the universe. Instead, the universe today appears to be dominated by a component with negative pressure, $P = -\rho$, often referred to as *dark energy*. For this case, from Eq. (2.21), we find that the energy density remains constant [15]:

$$\rho_\Lambda \propto a^0 = \text{constant}. \tag{2.28}$$

Since the energy density does not change with expansion, this implies that energy must be continuously generated as the universe expands.

Energy densities of different types of matter can be summarized as:

Component	**Equation of State,** $w = P/\rho$	**Energy Density,** $\rho(a)$
Dust	0	$\rho_m \propto a^{-3}$
Radiation	$1/3$	$\rho_r \propto a^{-4}$
Dark energy	-1	$\rho_\Lambda \propto a^0$

Table 2.1: Summary of different cosmic components, their equation-of-state parameter w, and the corresponding evolution of energy density with scale factor a.

2.6 Friedmann Equations

To relate the various matter components to the evolution of the scale factor in the Friedmann–Robertson–Walker (FRW) metric (2.1), we must compute the Einstein tensor on the left-hand side of the Einstein field equations,

$$G_{\mu\nu} = R_{\mu\nu} - \frac{1}{2} R\, g_{\mu\nu}, \tag{2.29}$$

where $R_{\mu\nu}$ is the Ricci tensor and R is the Ricci scalar [14, 10].

The Ricci tensor is defined as

$$R_{\mu\nu} \equiv \partial_\lambda \Gamma^\lambda_{\mu\nu} - \partial_\nu \Gamma^\lambda_{\mu\lambda} + \Gamma^\lambda_{\lambda\rho}\Gamma^\rho_{\mu\nu} - \Gamma^\rho_{\mu\lambda}\Gamma^\lambda_{\nu\rho}, \tag{2.30}$$

and the Ricci scalar is obtained by contraction,

$$R = R^{\mu}_{\ \mu} = g^{\mu\nu} R_{\mu\nu}. \tag{2.31}$$

The non-zero components of the Ricci tensor are then

$$R_{00} = -3\,\frac{\ddot{a}}{a}, \tag{2.32}$$

$$R_{ij} = \left[\frac{\ddot{a}}{a} + 2\left(\frac{\dot{a}}{a}\right)^2 + 2\,\frac{k}{a^2}\right] g_{ij}. \tag{2.33}$$

The Ricci scalar follows as

$$R = -6\left[\frac{\ddot{a}}{a} + \left(\frac{\dot{a}}{a}\right)^2 + \frac{k}{a^2}\right]. \tag{2.34}$$

Substituting these results into Eq. (2.29), we find the non-vanishing components of the Einstein tensor $G^{\mu}_{\ \nu} = g^{\mu\lambda} G_{\lambda\nu}$:

$$G^{0}_{\ 0} = 3\left[\left(\frac{\dot{a}}{a}\right)^2 + \frac{k}{a^2}\right], \tag{2.35}$$

$$G^{i}_{\ j} = \left[2\,\frac{\ddot{a}}{a} + \left(\frac{\dot{a}}{a}\right)^2 + \frac{k}{a^2}\right] \delta^{i}_{\ j}. \tag{2.36}$$

The dynamics of the universe are governed by the Einstein field equations [14],

$$G_{\mu\nu} = 8\pi G\, T_{\mu\nu}, \tag{2.37}$$

which relate the Einstein tensor $G_{\mu\nu}$ to the stress–energy tensor $T_{\mu\nu}$.

By combining Eqs. (2.35) and (2.36) with the stress–energy tensor from Eq. (2.17), we obtain the *Friedmann equations*, which govern the expansion dynamics of the universe [9, 12]:

$$\left(\frac{\dot{a}}{a}\right)^2 = \frac{8\pi G}{3}\,\rho - \frac{k}{a^2}, \tag{2.38}$$

$$\frac{\ddot{a}}{a} = -\,\frac{4\pi G}{3}\,(\rho + 3P). \tag{2.39}$$

The first Friedmann equation is often expressed in terms of the *Hubble parameter*,

$$H \equiv \frac{\dot{a}}{a}, \tag{2.40}$$

which gives

$$H^2 = \frac{8\pi G}{3}\rho - \frac{k}{a^2}. \tag{2.41}$$

For a spatially flat universe ($k = 0$), the corresponding *critical density* today is

$$\rho_{\text{crit},0} = \frac{3H_0^2}{8\pi G}. \tag{2.42}$$

where H_0 is the present-day Hubble parameter.

The Friedmann equation (2.38) can be expressed in terms of the present-day density parameters as

$$H^2(a) = H_0^2\left[\Omega_{r,0}\left(\frac{a_0}{a}\right)^4 + \Omega_{m,0}\left(\frac{a_0}{a}\right)^3 + \Omega_{k,0}\left(\frac{a_0}{a}\right)^2 + \Omega_{\Lambda,0}\right], \tag{2.43}$$

where the curvature density parameter is defined as $\Omega_{k,0} \equiv -\dfrac{k}{(a_0 H_0)^2}$. In most of the cosmological literature, the subscript '0' is omitted, such that quantities like Ω_m represent the present-day matter density fraction relative to the current critical density.

We typically adopt the normalization $a_0 = 1$. Under this convention, the Friedmann equation simplifies to [15]

$$\frac{H^2}{H_0^2} = \Omega_r a^{-4} + \Omega_m a^{-3} + \Omega_k a^{-2} + \Omega_\Lambda. \tag{2.44}$$

2.7 Single Component Universe

The distinct dependencies of radiation, matter, and vacuum energy on the scale factor are a^{-4}, a^{-3}, and a^0, respectively. Hence, throughout most of cosmic history, the Universe has been dominated by a single component at a time: first radiation, then matter, and finally dark energy (see Fig. 2.2) [9, 16]. We can describe each of these epochs using a constant equation-of-state parameter w_I, which efficiently characterizes all relevant cases.

For a spatially flat universe ($k = 0$) composed of a single component, the Friedmann equation (2.41) simplifies to

$$\frac{\dot{a}}{a} = H_0 \sqrt{\Omega_I}\, a^{-\frac{3}{2}(1+w_I)}, \tag{2.45}$$

where Ω_I denotes the corresponding density fraction [12]. Integrating Eq. (2.45),

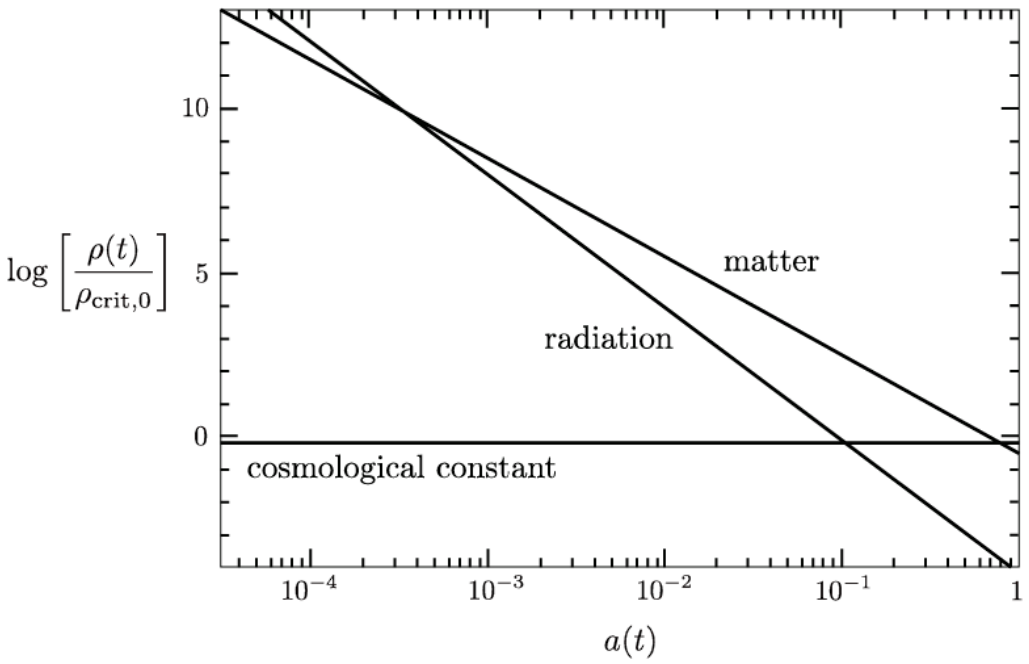

Figure 2.2: Evolution of the energy densities in the universe i.e. matter ($\propto a^{-3}$), radiation ($\propto a^{-4}$) and dark energy ($\propto a^0 = const.$) [17].

we obtain the time dependence of the scale factor:

$$a(t) \propto \begin{cases} t^{\frac{2}{3(1+w_I)}}, & w_I \neq -1, \\ t^{2/3}, & \text{(Matter domination; MD)}, \\ t^{1/2}, & \text{(Radiation domination; RD)}, \\ e^{Ht}, & w_I = -1 \quad \text{(Dark energy domination; } \Lambda\text{D)}. \end{cases} \tag{2.46}$$

In terms of conformal time τ, the scale factor evolves as

$$a(\tau) \propto \begin{cases} \tau^{\frac{2}{1+3w_I}}, & w_I \neq -1, \\ \tau^2, & \text{(Matter domination; MD)}, \\ \tau, & \text{(Radiation domination; RD)}, \\ (-\tau)^{-1}, & w_I = -1 \quad \text{(Dark energy domination; } \Lambda\text{D)}. \end{cases} \tag{2.47}$$

Table 2.2: Friedmann–Robertson–Walker (FRW) solutions for a flat, single-component universe.

Epoch	w	$\rho(a)$	$a(t)$
Radiation domination (RD)	$\frac{1}{3}$	a^{-4}	$t^{1/2}$
τ			
Matter domination (MD)	0	a^{-3}	$t^{2/3}$
τ^2			
Dark energy domination (ΛD)	-1	a^0	e^{Ht}
$(-\tau)^{-1}$			

2.8 Two Component Universe

Matter and radiation contributed equally to the total energy density when the scale factor was

$$a_{\text{eq}} \equiv \frac{\Omega_r}{\Omega_m} \approx 3 \times 10^{-4},$$

which occurred shortly before the emission of the cosmic microwave background (CMB) [12]. To describe the evolution of the Universe during this transition from radiation to matter domination, we consider a flat Friedmann–Robertson–Walker (FRW) universe containing both matter and radiation [9]. It is convenient to express the Friedmann equations in terms of conformal time τ. They then become

$$(a')^2 = \frac{8\pi G}{3}\,\rho\, a^4, \tag{2.48}$$

$$a'' = \frac{4\pi G}{3}\,(\rho - 3P)\, a^3, \tag{2.49}$$

where primes denote derivatives with respect to τ.

The total energy density is given by the sum of the matter and radiation components,

$$\rho = \rho_m + \rho_r = \frac{\rho_{\text{eq}}}{2}\left[\left(\frac{a_{\text{eq}}}{a}\right)^3 + \left(\frac{a_{\text{eq}}}{a}\right)^4\right], \tag{2.50}$$

where ρ_{eq} is the total energy density at matter–radiation equality [9].

Since radiation satisfies $\rho_r - 3P_r = 0$, it does not appear in the source term of Eq. (2.49). Moreover, matter obeys $\rho_m a^3 = \text{const.} = \frac{1}{2}\rho_{\text{eq}} a_{\text{eq}}^3$, so Eq. (2.49) reduces to

$$a'' = \frac{2\pi G}{3}\,\rho_{\text{eq}} a_{\text{eq}}^3. \tag{2.51}$$

Integrating Eq. (2.51) gives

$$a(\tau) = \frac{\pi G}{3}\,\rho_{\mathsf{eq}} a_{\mathsf{eq}}^3 \tau^2 + C\tau + D. \tag{2.52}$$

Applying the boundary condition $a(\tau = 0) = 0$ fixes $D = 0$. Substituting Eq. (2.52) and Eq. (2.50) into Eq. (2.48) determines the remaining constant,

$$C = \left(\frac{4\pi G}{3}\,\rho_{\mathsf{eq}} a_{\mathsf{eq}}^4\right)^{1/2}. \tag{2.53}$$

Thus, the solution for the scale factor can be written as

$$a(\tau) = a_{\mathsf{eq}}\left[\left(\frac{\tau}{\tau_*}\right)^2 + 2\left(\frac{\tau}{\tau_*}\right)\right], \tag{2.54}$$

where

$$\tau_* \equiv \left(\frac{\pi G}{3}\rho_{\mathsf{eq}} a_{\mathsf{eq}}^2\right)^{-1/2} = \frac{\tau_{\mathsf{eq}}}{\sqrt{2}-1}. \tag{2.55}$$

In the early-time limit $\tau \ll \tau_{\mathsf{eq}}$, Eq. (2.54) approaches the radiation-dominated behavior $a \propto \tau$. Whereas for $\tau \gg \tau_{\mathsf{eq}}$, the matter-dominated scaling $a \propto \tau^2$ is recovered.

2.9 Particle Horizon & Event Horizon

The maximum comoving distance that light can travel between an initial time t_i and a later time t is given by

$$\chi_p(\tau) = \tau - \tau_i = \int_{t_i}^{t} \frac{dt'}{a(t')}. \tag{2.56}$$

This quantity is known as the *(comoving) particle horizon* [11]. The initial time t_i is often identified with the *origin of the Universe*, corresponding to the initial singularity where

$$a(t_i = 0) = 0.^1$$

The corresponding *physical* size of the particle horizon is

$$d_p(t) = a(t)\,\chi_p(\tau). \tag{2.57}$$

[1] Whether $t_i = 0$ also corresponds to $\tau_i = 0$ depends on the evolution of the scale factor $a(t)$; for instance, during inflation $t_i = 0$ does not correspond to $\tau_i = 0$.

The particle horizon plays a crucial role in understanding the causal structure of the Universe and will be central to our later discussion of cosmic inflation [16]. In the standard Big Bang model, the Universe has a finite age. It begins at a definite time in the past and thus, the particle horizon at any finite time is also finite. This imposes a limit on the maximum distance over which different regions of spacetime could have been in causal contact.

This limitation lies at the core of the so-called *Big Bang puzzles*, such as the *horizon problem*, which inflationary cosmology was introduced to resolve [3].

An *event horizon* defines the boundary separating events whose signals, emitted at a given conformal time τ, can ever reach an observer in the future from those that can never do so. In comoving coordinates, the points that lie beyond this horizon satisfy

$$\chi > \chi_e = \int_{\tau}^{\tau_{\max}} d\tau' = \tau_{\max} - \tau, \tag{2.58}$$

where $\tau_{\max}$ represents the *final moment of time*, which may be either finite or infinite depending on the cosmological model [9].

The corresponding *physical size* of the event horizon is given by

$$d_e(t) = a(t)\,\chi_e. \tag{2.59}$$

The event horizon thus depicts the ultimate causal boundary for an observer: no information emitted from beyond this surface at time τ will ever be received, even in the infinite future [11].

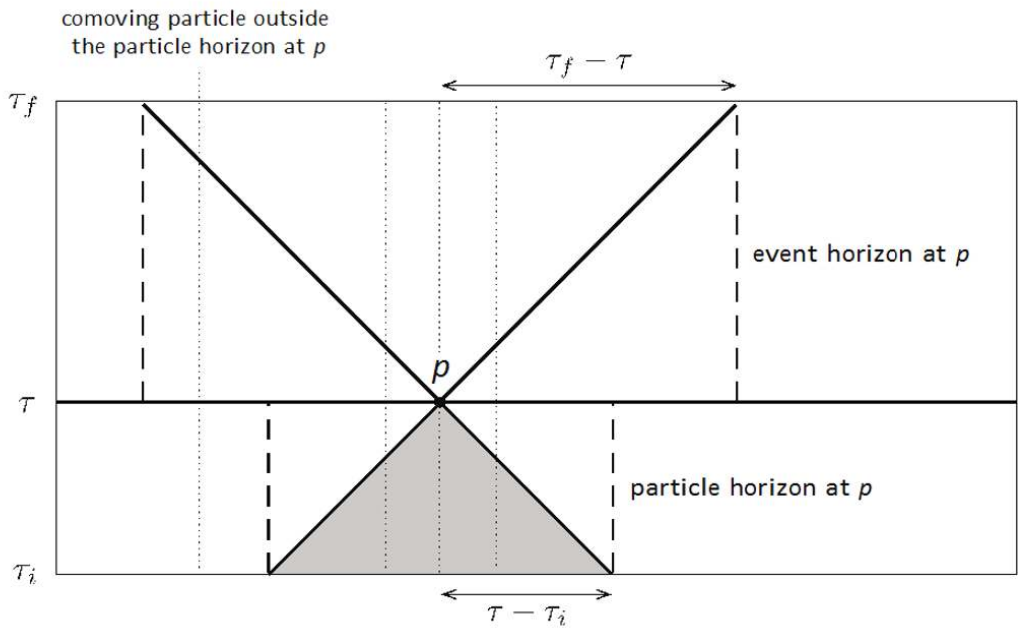

Figure 2.3: Spacetime diagram illustrating the concept of horizons. Dotted lines show the worldlines of comoving objects. The event horizon is the maximal distance to which we can send signal. The particle horizon is the maximal distance from which we can receive signals [17].

Chapter 3

Inflationary Cosmology

3.1 Horizon Problem (Uniformity of CMB)

In the previous section, we introduced the comoving (or particle) horizon τ as the causal limit of the Universe, i.e., the maximum comoving distance that a light signal can traverse between the initial time $t = 0$ and a later time t [9, 13]. It is defined as

$$\tau \equiv \int_0^t \frac{dt'}{a(t')} = \int_0^a \frac{da'}{a'^2 H(a')} = \int_0^a \frac{d\ln a'}{a' H(a')}. \tag{3.1}$$

Thus, the comoving horizon can be expressed as an integral over the *comoving Hubble radius*, $(aH)^{-1}$, which plays a key role in the study of inflationary dynamics [18].

For a universe dominated by a single fluid characterized by an equation of state $P = w\rho$, the comoving Hubble radius scales as

$$(aH)^{-1} = H_0^{-1}\, a^{\frac{1}{2}(1+3w)}, \quad \text{[Assuming spatial curvature, } k \simeq 0] \tag{3.2}$$

The exponent clearly depends on the combination $(1 + 3w)$, determining the qualitative evolution of $(aH)^{-1}$ [10].

During the standard Big Bang expansion, where $w \gtrsim 0$, the quantity $(aH)^{-1}$ increases monotonically with a. Consequently, the comoving horizon τ, which represents the fraction of the universe in causal contact, also grows with time:

$$\tau \propto a^{\frac{1}{2}(1+3w)}. \tag{3.3}$$

Once again, the sign of $(1+3w)$ dictates whether the comoving horizon expands or contracts.

Specifically, for the radiation-dominated (RD) and matter-dominated (MD) epochs, we obtain

$$\tau = \int_0^a \frac{da'}{a'^2 H(a')} \propto \begin{cases} a, & \text{(RD)} \\ a^{1/2}, & \text{(MD)} \end{cases} . \tag{3.4}$$

The finiteness of the causal distance between the initial time $t_i = 0$ and the epoch of recombination $t_{\rm rec}$ presents a profound issue in standard cosmology. It implies that most regions observed in the cosmic microwave background (CMB) have past light cones that never overlapped [12]. This means they were never in causal contact prior to photon decoupling. Despite this, the CMB is observed to

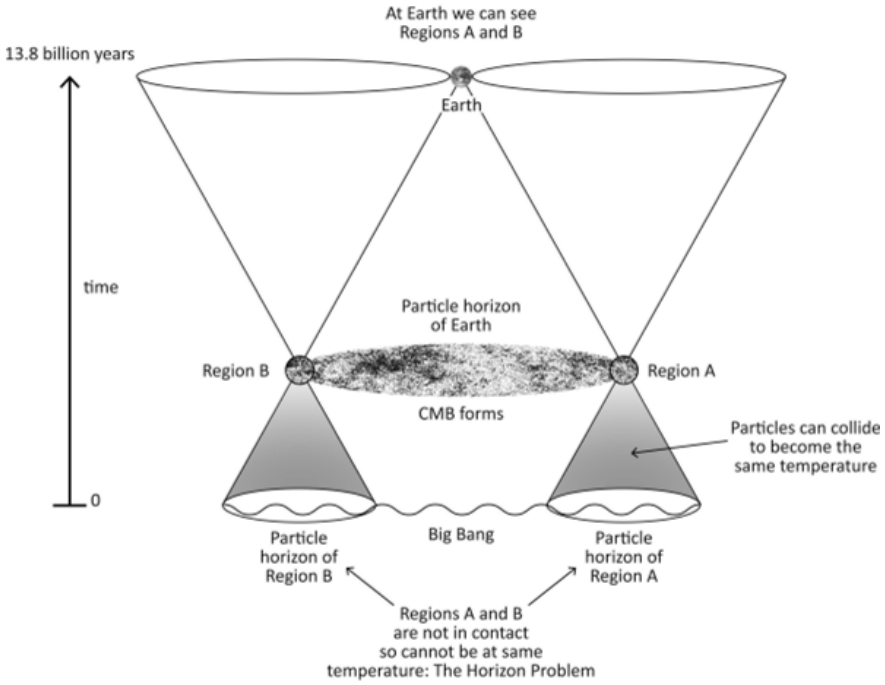

Figure 3.1: The horizon problem in the conventional Big Bang model [19].

be extraordinarily isotropic, with temperature fluctuations smaller than one part in ten thousand [1]. This raises a puzzling question: how can photons arriving from widely separated regions of the sky possess almost identical temperatures? These causally-disconnected regions could never have exchanged information. In particular, points in the CMB sky separated by more than about one degree should not have been in causal contact according to the standard Big Bang model.

The observed uniformity of the CMB extends across scales much larger than the particle horizon at the time of recombination. Indeed, within the framework

of conventional cosmology, the CMB would consist of roughly 10^4 causally disconnected patches [13]. If these regions could not have communicated with one another, why do they appear so homogeneous?

This apparent contradiction between the observed isotropy of the CMB and the finite causal structure of the early universe is known as the *horizon problem*.

3.2 Flatness Problem (Universe is astonishingly flat)

In General Relativity, spacetime is dynamical and it curves in response to the distribution of matter and energy [10]. Given this, one may ask: why is the Universe observed to be so nearly flat, resembling Euclidean space? To make this question precise, let us recall the Friedmann equation

$$H^2 = \frac{1}{3}\rho(a) - \frac{k}{a^2}, \tag{3.5}$$

which can be conveniently rewritten as

$$1 - \Omega(a) = -\frac{k}{(aH)^2}, \tag{3.6}$$

where

$$\Omega(a) \equiv \frac{\rho(a)}{\rho_{\text{crit}}(a)}, \quad \rho_{\text{crit}}(a) \equiv 3H(a)^2. \tag{3.7}$$

e standard Big Bang cosmology, the comoving Hubble radius $(aH)^{-1}$ increases with time [18]. From Eq. (3.6), this implies that $|\Omega - 1|$ diverges as the Universe evolves. Hence, the near-flatness observed today, $\Omega(a_0) \simeq 1$, requires an extraordinarily precise fine-tuning of Ω to be extremely close to unity in the early Universe [13, 9].

Using Eq. (3.2) and differentiating Eq. (3.6) yields

$$\frac{d\Omega}{d\ln a} = (1+3w)\Omega(\Omega - 1), \tag{3.8}$$

where w is the equation-of-state parameter of the dominant energy component. For $1 + 3w > 0$ (which holds for all forms of "ordinary" matter), a flat Universe ($\Omega = 1$) corresponds to an unstable equilibrium [12]. That is,

$$\frac{d|\Omega - 1|}{d\ln a} = (1+3w)\Omega|\Omega - 1| > 0. \text{ (Polarity does not invert around } \Omega = 1) \tag{3.9}$$

Therefore, a small deviation of Ω from 1 leads to a rapid departure, either towards a collapse ($\Omega \to \infty$) or towards complete emptying ($\Omega \to 0$). Yet we know that today $\Omega(a_0) \simeq 1$.

Now, the question remains: why has the Universe always been this flat? This is known as the *flatness problem* [3, 4].

3.3 Inflation as a Solution

In the previous two sections, we highlighted the central importance of the comoving Hubble radius, $(aH)^{-1}$, in understanding the horizon and flatness problems of the standard Big Bang cosmology [9, 13]. Both of these issues stem from the fact that, within the conventional framework, the comoving Hubble radius increases monotonically with time [18]. This observation naturally suggests an elegant resolution: reverse the behavior of the comoving Hubble radius so that it decreases sufficiently during an early epoch of the Universe.

We therefore hypothesize that the Universe experienced a phase of accelerated expansion in its earliest moments, a period known as *inflation* [3, 4, 5]. The term "very early" refers to an epoch preceding the electroweak phase transition, although its precise timing remains uncertain with our current understanding.

3.3.1 Solution to the Horizon Problem

For a decreasing Hubble sphere, the integral in Eq. (3.1) is dominated by its lower limit. As a result, the Big Bang singularity is shifted to negative conformal time [13],

$$\tau_i = \frac{2H_0^{-1}}{1+3w}\, a_i^{\frac{1}{2}(1+3w)} \xrightarrow{a_i \to 0, w < -\frac{1}{3}} -\infty. \tag{3.10}$$

This means that there exists much more conformal time between the singularity and decoupling than previously assumed.

In this framework, the past light cones of distant regions in the CMB have sufficient time to intersect before the epoch corresponding to τ_i [9]. Hence, the remarkable isotropy of the CMB no longer poses a paradox. In the inflationary picture, $\tau = 0$ does not mark the initial singularity but rather represents the transition point between the inflationary epoch and the standard Big Bang evolution. Thus, conformal time extends both before and after $\tau = 0$.

Recall the definition of the comoving horizon (= conformal time) as a logarithmic integral of the comoving Hubble radius shown in Eq. (3.1). The *comoving*

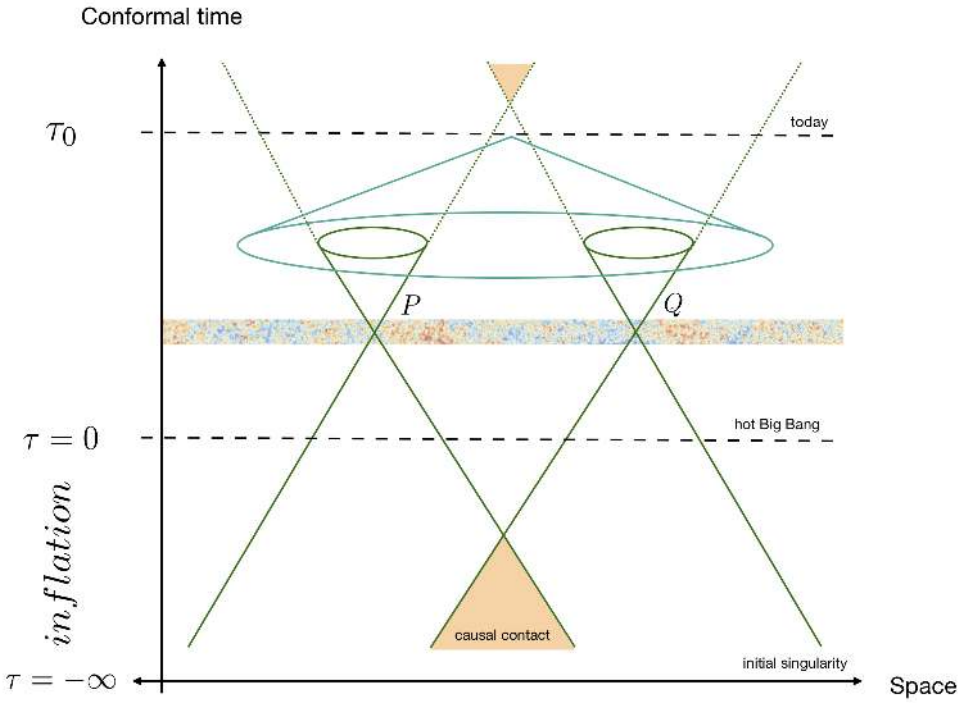

Figure 3.2: Inflationary solution to the horizon problem. Two CMB points, P and Q, which are causally disconnected now, were in thermal equilibrium at some point in the past, thus solving the horizon problem [20].

Hubble radius, $(aH)^{-1}$, represents the comoving distance at which the recession velocity due to cosmic expansion equals the speed of light [13]. It therefore serves as a measure of causal connectivity between particles: by comparing the comoving separation λ of two particles with $(aH)^{-1}$, one can determine whether they can communicate at a given epoch.

It is important to note that the comoving Hubble radius $(aH)^{-1}$ and the particle horizon $\chi_{\rm ph}$ are conceptually distinct [18]:

- If $\lambda > \chi_{\rm ph}$, the two particles have *never* been in causal contact.
- If $\lambda > (aH)^{-1}$, the particles cannot exchange signals at the present time.

This distinction plays a crucial role in addressing the horizon problem. It is possible that the conformal time τ is much larger than $(aH)^{-1}$ today [13]. It implies that particles are no longer in causal contact, but that they were in causal contact in the early universe. From Eq. (3.1), this situation can occur if the comoving Hubble radius in the early universe was much larger than its current value, so that τ accumulated most of its contribution from early times.

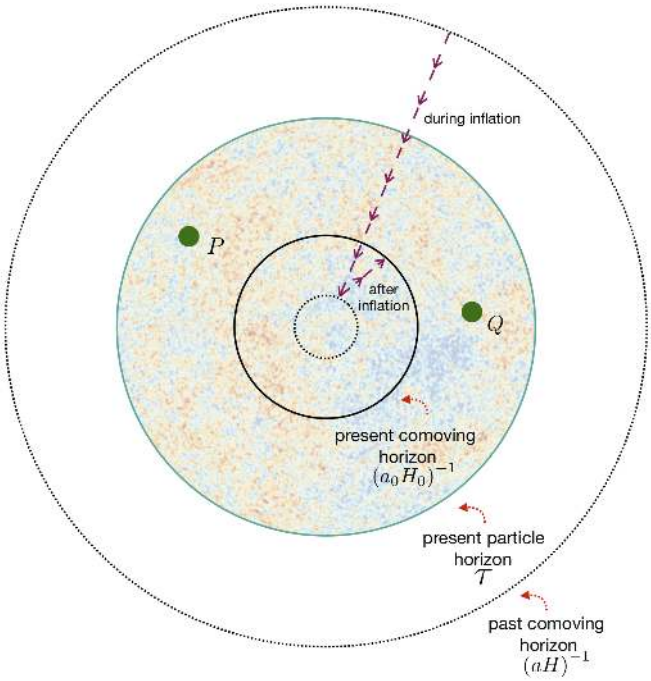

Figure 3.3: Evolution of the Particle horizon and comoving Hubble radius in the inflationary universe, before and after inflation. Two particles, P and Q are not in causal contact in present time, but they could exchange information before the inflationary period [20].

3.3.2 Solution to the Flatness Problem

Recall the Friedmann equation for a non-flat universe in Section 3.2,

$$1 - \Omega(a) = -\frac{k}{(aH)^2}.$$

In the standard Big Bang cosmology, the comoving Hubble radius $(aH)^{-1}$ increases with time, leading to a divergence of $|1-\Omega|$ [9]. As a result, the universe must have started off extremely close to flatness in the early epochs to remain nearly flat today — a severe fine-tuning known as the *flatness problem* [10].

During inflation, however, the situation changes dramatically. The Hubble parameter H remains nearly constant while the scale factor a grows exponentially [13]. Consequently, the comoving Hubble radius $(aH)^{-1}$ decreases rapidly. From the equation, we see that as $(aH)^{-1}$ shrinks, the term $|1-\Omega|$ is driven toward zero, irrespective of its initial value.

Therefore, inflation dynamically drives the universe toward spatial flatness.

The solution $\Omega = 1$ is no longer a finely tuned initial condition but an *attractor* solution during the inflationary phase [18]. This elegant mechanism provides a natural resolution to the flatness problem of the standard Big Bang cosmology.

3.3.3 Conditions for Inflation

Accelerated Expansion. Starting from the time derivative of the comoving Hubble radius, we have

$$\frac{d}{dt}(aH)^{-1} = \frac{d}{dt}(\dot{a})^{-1} = -\frac{\ddot{a}}{\dot{a}^2}. \tag{3.11}$$

From this relation, it follows that a *decreasing* comoving Hubble radius corresponds to an *accelerating* expansion of the universe [13, 21],

$$\ddot{a} > 0. \tag{3.12}$$

Hence, inflation can equivalently be defined as a period during which the scale factor undergoes accelerated growth [22].

Slowly-Varying Hubble Parameters. Alternatively, the rate of change of the comoving Hubble radius can be expressed as

$$\frac{d}{dt}(aH)^{-1} = -\frac{a\dot{H} + aH^2}{(aH)^2} = -\frac{1}{a}(1 - \epsilon_H), \tag{3.13}$$

where we have introduced the *first slow-roll parameter* [23]

$$\epsilon_H \equiv -\frac{\dot{H}}{H^2} = \frac{-d\ln H}{dN}. \tag{3.14}$$

Here, we define the differential number of e-folds as

$$dN \equiv d\ln a = H\,dt, \tag{3.15}$$

which quantifies the logarithmic growth of the scale factor during inflation. Eq. (3.14) then implies that the fractional change of the Hubble parameter per e-fold is small.

A shrinking comoving Hubble radius thus requires

$$\epsilon_H < 1. \tag{3.16}$$

To successfully resolve the horizon problem, inflation must last for a sufficiently long duration—typically between $N \sim 40$ and 60 e-folds of exponential expansion [13, 18]. This requires the first slow-roll parameter ϵ_H to remain small over many Hubble times.

To measure how slowly ϵ_H evolves, we introduce a *second slow-roll parameter*,

$$\eta_H \equiv \frac{d\ln \epsilon_H}{dN} = \frac{\dot{\epsilon_H}}{H\,\epsilon_H}. \tag{3.17}$$

When $|\eta_H| < 1$, the fractional change of ϵ_H per Hubble time is small, ensuring that inflation continues for a prolonged period [22, 13]. These conditions characterize the inflationary regime, in which the expansion of the universe is accelerating and the Hubble parameters vary very slowly with time.

3.4 Single field inflation

3.4.1 Background Dynamics

The simplest models of inflation introduce a single scalar field, the *inflaton* ϕ [22, 13]. Although the precise physical origin of ϕ is unspecified, it serves as an order parameter or an effective clock that characterizes the time evolution of the inflationary energy density.

The dynamics of a scalar field minimally coupled to gravity is governed by the action [13, 10]

$$S = \int d^4x\,\sqrt{-g}\left[\frac{1}{2}\mathcal{R} + \frac{1}{2}g^{\mu\nu}\partial_\mu\phi\,\partial_\nu\phi - V(\phi)\right] = S_{\rm EH} + S_\phi, \tag{3.18}$$

where $S_{\rm EH}$ is the Einstein–Hilbert action, S_ϕ represents the action of a scalar field with a canonical kinetic term, and $\mathcal{R}$ is the comoving curvature perturbation. The potential $V(\phi)$ encodes the self-interaction of the field.

The corresponding energy–momentum tensor is obtained as [9]

$$T^{(\phi)}_{\mu\nu} \equiv -\frac{2}{\sqrt{-g}}\frac{\delta S_\phi}{\delta g^{\mu\nu}} = \partial_\mu\phi\,\partial_\nu\phi - g_{\mu\nu}\left(\frac{1}{2}\partial_\sigma\phi\,\partial^\sigma\phi + V(\phi)\right). \tag{3.19}$$

The equation of motion for the scalar field follows from the minimization of the action:

$$\frac{\delta S_\phi}{\delta\phi} = \frac{1}{\sqrt{-g}}\,\partial_\mu\big(\sqrt{-g}\,\partial^\mu\phi\big) + V_{,\phi} = 0, \qquad \text{where } \; V_{,\phi} \equiv dV/d\phi. \tag{3.20}$$

which can be rewritten as

$$\ddot{\phi} - \frac{\nabla^2\phi}{a^2} + 3H\dot{\phi} + V_{,\phi} = 0 \tag{3.21}$$

The homogeneity and isotropy of the background universe restricts ϕ to be only time-dependent. Hence, $\phi(t, \mathbf{x}) \equiv \phi(t)$, $\nabla^2\phi = 0$ and hence the energy-momentum tensor becomes diagonal

$$T^0_0 = \rho_\phi = \frac{1}{2}\dot{\phi}^2 + V(\phi), \tag{3.22a}$$

$$T^i_j = -p_\phi \delta^i_j = -\left[\frac{1}{2}\dot{\phi}^2 - V(\phi)\right]\delta^i_j. \tag{3.22b}$$

The corresponding equation of state is

$$w_\phi \equiv \frac{p_\phi}{\rho_\phi} = \frac{\frac{1}{2}\dot{\phi}^2 - V(\phi)}{\frac{1}{2}\dot{\phi}^2 + V(\phi)}. \tag{3.23}$$

A scalar field can thus generate negative pressure ($w_\phi < 0$) and accelerated expansion ($w_\phi < -1/3$) whenever the potential energy $V(\phi)$ dominates over the kinetic energy $\frac{1}{2}\dot{\phi}^2$. The coupled evolution of the homogeneous scalar field and the FRW background is described by [24]

$$\ddot{\phi} + 3H\dot{\phi} + V_{,\phi} = 0, \tag{3.24}$$

$$H^2 = \frac{1}{3}\left(\frac{1}{2}\dot{\phi}^2 + V(\phi)\right). \tag{3.25}$$

For large values of the potential, the expansion rate H is significant, and the term $3H\dot{\phi}$ provides strong *Hubble friction* that slows the field's motion.

3.4.2 Quantum Fluctuations

Curvature Perturbation

A convenient gauge which we will use, is known as the *longitudinal gauge* (also called the conformal Newtonian gauge) [9, 12]. In this gauge, the FRW metric will be [1]

$$ds^2 = (1 + 2\Phi)\, dt^2 - a^2(t)(1 - 2\Psi)\, d\mathbf{x}^2. \tag{3.26}$$

[1] More details can be found in Section 12.2 and Appendix B of *TASI Lectures in Inflation, Daniel Baumann* [13].

where Φ ($\propto \mathcal{A}$) and Ψ ($\propto \psi$) are the two independent functions which are called *Bardeen potentials*. For the above metric, the equation of motion of the Bardeen potential [25]

$$\Phi'' + 3\mathcal{H}(1+c_A^2)\Phi' - c_A^2\nabla^2\Phi + \left[2\mathcal{H}' + (1+3c_A^2)\mathcal{H}^2\right]\Phi = 4\pi G a^2 \delta p^{\rm NA}. \quad (3.27)$$

where $\mathcal{H} = (a'/a)$ is the conformal Hubble parameter.

Let us consider the scalar field ϕ is perturbed by a factor of $\delta\phi$ from its average value. From Eq. (3.22) and using the metric (3.26), the perturbed stress-energy tensor will be

$$\delta T^0_0 = \dot{\phi}\,\dot{\delta\phi} - \dot{\phi}^2\Phi + V_{,\phi}\,\delta\phi = \delta\rho, \quad (3.28a)$$

$$\delta T^0_i = \nabla_i(\dot{\phi}\,\delta\phi) = \nabla_i(\delta\sigma), \quad (3.28b)$$

$$\delta T^i_j = -\left(\dot{\phi}\,\dot{\delta\phi} - \dot{\phi}^2\Phi - V_{,\phi}\,\delta\phi\right)\delta^i_j = -\delta p\,\delta^i_j. \quad (3.28c)$$

We are interested in the evolution of a particular quantity called *curvature perturbation* [26, 27].

$$\mathcal{R} \equiv \Phi + \left(\frac{2\rho}{3\mathcal{H}}\right)\left(\frac{\Phi' + \mathcal{H}\Phi}{\rho + p}\right). \quad (3.29)$$

And it's derivative

$$\mathcal{R}'_k = -\left(\frac{\mathcal{H}}{\mathcal{H}^2 - \mathcal{H}'}\right)k^2\Phi_k. \quad (3.30)$$

Curvature perturbation is very important because this provides the essential link between the fluctuations created by inflation and the fluctuations that we observe in the CMB.

Now we can rewrite the equation of motion of Bardeen potential (3.27) in terms of curvature perturbation as [27]

$$\mathcal{R}''_k + 2\left(\frac{z'}{z}\right)\mathcal{R}'_k + k^2\mathcal{R}_k = 0, \quad (3.31)$$

where the quantity z encodes the background dynamics and is defined as

$$z \equiv a\frac{\dot{\phi}}{H} = a\frac{\phi'}{\mathcal{H}}. \quad (3.32)$$

Introducing another variable known as the *Mukhanov–Sasaki variable*

$$v \equiv z\mathcal{R}, \quad (3.33)$$

In Fourier space, Eq. (3.31) becomes

$$v_k'' + \left(k^2 - \frac{z''}{z}\right) v_k = 0, \tag{3.34}$$

which is referred to as the *Mukhanov–Sasaki equation for curvature perturbation* [27, 9].

Tensor Perturbation

Tensor perturbations are important because they are responsible for generation of the primordial gravitational waves [13, 28].

The perturbed FRW metric including tensor perturbations can be written as [2]

$$ds^2 = dt^2 - a^2(t)\left(\delta_{ij} + h_{ij}\right) dx^i dx^j, \tag{3.35}$$

where h_{ij} is a symmetric, transverse, and traceless tensor describing gravitational waves. These tensor perturbations contain two independent degrees of freedom, corresponding to the two polarization states of gravitational waves.

Using the metric (3.35), the components of the perturbed Einstein tensor are found to be

$$\delta G_0^0 = \delta G_i^0 = 0, \tag{3.36}$$

$$\delta G_j^i = -\left(\frac{1}{2}\right)\left[\ddot{h}_j^i + 3H\dot{h}_j^i - \frac{1}{a^2}\nabla^2 h_j^i\right]. \tag{3.37}$$

In the absence of anisotropic stress perturbations, i.e. when $\delta T_j^i = 0$, the tensor perturbation equation simplifies to [9]

$$h_{ij}'' + 2\mathcal{H}h_{ij}' - \nabla^2 h_{ij} = 0, \tag{3.38}$$

where h_{ij} represents the amplitude of the gravitational wave. This equation shows that gravitational waves can propagate freely even in the absence of matter sources [10]. We can decompose the tensor perturbation $h_{ij}(\tau, \mathbf{x})$ into its Fourier modes and polarization states as

$$h_{ij}(\tau, \mathbf{x}) = \sum_{s=+,\times} \int \frac{d^3k}{(2\pi)^{3/2}}\, \epsilon_{ij}^{(s)}(\mathbf{k})\, h_k^{(s)}(\tau)\, e^{i\mathbf{k}\cdot\mathbf{x}}, \tag{3.39}$$

[2] More details can be found in Section 5.3 of *Modern Cosmology, Scott Dodelson* [12]

where $\epsilon_{ij}^{(s)}(\mathbf{k})$ are the polarization tensors satisfying the transverse and traceless conditions,

$$k^i \epsilon_{ij}^{(s)} = 0, \quad \epsilon_{\ i}^{i(s)} = 0, \quad \epsilon_{ij}^{(s)}(\mathbf{k})\, \epsilon^{ij(s')*}(\mathbf{k}) = 2\delta_{ss'}. \tag{3.40}$$

Each polarization mode $h_k^{(s)}$ satisfies the same evolution equation due to statistical isotropy. If we define $h = u/a$, then Eq. (3.38) can be rewritten as [9]

$$u_k'' + \left(k^2 - \frac{a''}{a}\right) u_k = 0, \tag{3.41}$$

which is the *Mukhanov–Sasaki equation for tensor perturbations* [27].

3.4.3 Quantization and Power Spectra

During inflation, the background scalar field is treated as a classical quantity, while only the perturbations around its mean value are quantized [9, 13]. In the framework of quantum field theory, the variable $\mathcal{R}$ and its conjugate momentum π are promoted to operators $\hat{\mathcal{R}}$ and $\hat{\pi}$, which obey the equal-time commutation relations [3]

$$\begin{aligned} [\hat{\mathcal{R}}(\eta_H, \mathbf{x}), \hat{\mathcal{R}}(\eta_H, \mathbf{y})] &= [\hat{\pi}(\eta_H, \mathbf{x}), \hat{\pi}(\eta_H, \mathbf{y})] = 0, \\ [\hat{\mathcal{R}}(\eta_H, \mathbf{x}), \hat{\pi}(\eta_H, \mathbf{y})] &= i\, \delta(\mathbf{x} - \mathbf{y}), \end{aligned} \tag{3.42}$$

where we have set $\hbar = 1$.

The curvature perturbation operator can be expanded in terms of its Fourier modes as

$$\hat{\mathcal{R}}(\eta_H, \mathbf{x}) = \int \frac{d^3\mathbf{k}}{(2\pi)^{3/2}} \left[\hat{a}_{\mathbf{k}} \mathcal{R}_k(\eta_H) e^{i\mathbf{k}\cdot\mathbf{x}} + \hat{a}_{\mathbf{k}}^\dagger \mathcal{R}_k^*(\eta_H) e^{-i\mathbf{k}\cdot\mathbf{x}}\right], \tag{3.43}$$

where $\hat{a}_{\mathbf{k}}$ and $\hat{a}_{\mathbf{k}}^\dagger$ are the annihilation and creation operators, respectively. These operators satisfy the commutation relations [10]

$$[\hat{a}_{\mathbf{k}}, \hat{a}_{\mathbf{k}'}] = [\hat{a}_{\mathbf{k}}^\dagger, \hat{a}_{\mathbf{k}'}^\dagger] = 0, \qquad [\hat{a}_{\mathbf{k}}, \hat{a}_{\mathbf{k}'}^\dagger] = \delta(\mathbf{k} - \mathbf{k}'), \tag{3.44}$$

and the mode function $\mathcal{R}_k(\eta_H)$ satisfies Eq. (3.31). The vacuum state $|0\rangle$ is defined by the condition

$$\hat{a}_{\mathbf{k}} |0\rangle = 0. \tag{3.45}$$

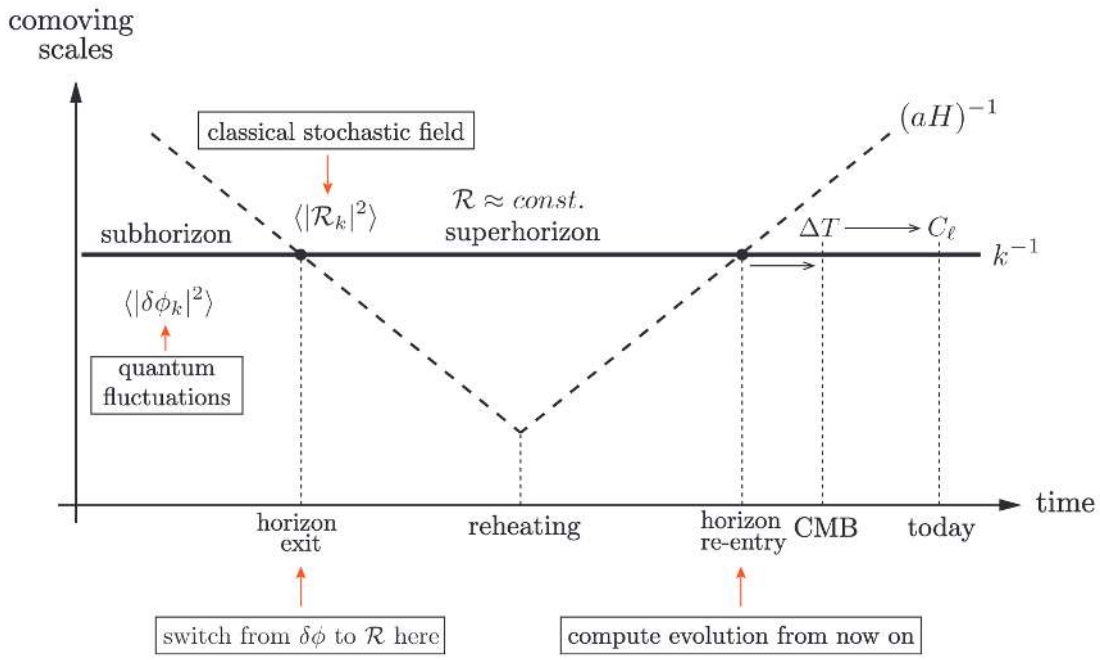

Figure 3.4: Creation and evolution of perturbations in the inflationary universe. Fluctuations are generated on subhorizon scales. As the comoving Hubble radius $(aH)^{-1}$ shrinks, these perturbations exit the horizon and freeze, remaining constant until they re-enter at later times [13].

Fluctuations are generated across all length scales, corresponding to a spectrum of wavenumbers k [12]. Cosmologically relevant perturbations initially exist well inside the Hubble radius, i.e., in the *sub-horizon* regime:

$$k \gg aH. \tag{3.46}$$

During inflation, while the comoving wavenumber k remains constant, the comoving Hubble radius $(aH)^{-1}$ decreases. Eventually all modes cross outside the horizon, which is denoted as *horizon exit*. Thus, modes enter the *super-horizon* regime:

$$k \ll aH. \tag{3.47}$$

In the context of linear perturbation theory, the perturbations are expected to be Gaussian. For a Gaussian random field, all statistical information is encoded in the two-point correlation function [9]. In cosmology, this is conveniently expressed

[3] More *details can be found in Section 6.4 and 6.5 of Cosmology Part III Mathematical Tripos, Daniel Baumann* [17]

through the *power spectrum*. The scalar and tensor power spectra are defined by

$$\langle 0|\hat{\mathcal{R}}_{\mathbf{k}}(\eta_H)\,\hat{\mathcal{R}}_{\mathbf{k}'}(\eta_H)|0\rangle = \frac{2\pi^2}{k^3}\,\mathcal{P}_{\mathcal{R}}(k)\,\delta^{(3)}(\mathbf{k}+\mathbf{k}'), \tag{3.48}$$

where $\mathcal{P}_{\mathcal{R}}(k)$ is the scalar power spectrum. Using Eq. (3.43), one can relate the power spectrum to the mode functions as

$$\mathcal{P}_{\mathcal{R}}(k) = \frac{k^3}{2\pi^2}|\mathcal{R}_k|^2 = \frac{k^3}{2\pi^2}\frac{|v_k|^2}{z^2}. \tag{3.49}$$

Similarly, the tensor power spectrum can be expressed in terms of the tensor mode functions h_k or u_k as

$$\mathcal{P}_T(k) = 4\left(\frac{k^3}{2\pi^2}\right)|h_k|^2 = 4\left(\frac{k^3}{2\pi^2}\right)\frac{|u_k|^2}{a^2} \tag{3.50}$$

These spectra are evaluated in the super-horizon limit, where the curvature perturbation effectively becomes constant [13].

Another important quantity is the spectral index, which characterizes the scale dependence of the power spectrum. It is conventionally defined as

$$n_S - 1 \equiv \frac{d\ln\mathcal{P}_{\mathcal{R}}}{d\ln k}, \qquad n_T \equiv \frac{d\ln\mathcal{P}_T}{d\ln k}. \tag{3.51}$$

If the spectrum remains constant at super-horizon scale (scale-invariant spectrum), this corresponds to $n_S = 1$ and $n_T = 0$, indicating that the spectrum does not vary with scale.

Finally, the tensor-to-scalar ratio is defined as

$$r(k) \equiv \frac{\mathcal{P}_T(k)}{\mathcal{P}_{\mathcal{R}}(k)}. \tag{3.52}$$

Both the spectral indices and the tensor-to-scalar ratio are fundamental inflationary parameters that can be constrained by observations [12, 9].

3.4.4 Bunch-Davies Initial Conditions

The initial conditions for the perturbation modes must be set in the far past, when all comoving scales were deep inside the Hubble radius, i.e., $\tau \to -\infty$ or $k \gg aH$. At scales much smaller than the Hubble radius, the curvature of

spacetime becomes negligible, and the dynamics reduce to that of Minkowski space [13]. In this limit, the Mukhanov-Sasaki equation (3.34) simplifies to

$$v_k'' + k^2 v_k = 0, \tag{3.53}$$

which describes a simple harmonic oscillator with constant frequency k.

The positive-frequency solutions for the mode functions in this limit are

$$\lim_{k \gg aH} (v_k(\tau), u_k(\tau)) = \frac{1}{\sqrt{2k}} e^{-ik\tau}, \tag{3.54}$$

which defines the initial conditions for the perturbations. The corresponding vacuum state associated with these modes is known as the *Bunch-Davies vacuum* [9].

3.5 Slow-roll Inflation

3.5.1 Dynamics

The acceleration equation for a universe dominated by a homogeneous scalar field ϕ can be expressed as

$$\frac{\ddot{a}}{a} = -\frac{1}{6}(\rho_\phi + 3p_\phi) = H^2(1 - \epsilon_H), \tag{3.55}$$

where

$$\epsilon_H \equiv \frac{3}{2}(1 + w_\phi) = \frac{1}{2}\frac{\dot{\phi}^2}{H^2}. \tag{3.56}$$

Accelerated expansion occurs when $\epsilon_H < 1$. In the *de Sitter* limit, where $p_\phi \to -\rho_\phi$ (hence $\omega_\phi = -1$), we have $\epsilon_H \to 0$. In this regime, the potential energy dominates over the kinetic term, i.e.

$$\dot{\phi}^2 \ll V(\phi).$$

A prolonged phase of accelerated expansion (inflation) requires the scalar field's second derivative to be sufficiently small,

$$|\ddot{\phi}| \ll |3H\dot{\phi}|, |V_{,\phi}|. \tag{3.57}$$

This condition ensures the validity of the slow-roll approximation and introduces the dimensionless acceleration per Hubble time

$$\delta \equiv -\frac{\ddot{\phi}}{H\dot{\phi}} = \epsilon_H - \frac{1}{2}\frac{\dot{\epsilon_H}}{H\,\epsilon_H} = \epsilon_H + \frac{1}{2}|\eta_H|, \tag{3.58}$$

where $|\delta| < 1$ guarantees that the fractional change of ϵ_H per e-fold (2nd slow-roll parameter, η_H) is small [29, 13].

The slow-roll conditions are thus

$$\epsilon_H,\, |\eta_H| \ll 1, \quad \therefore |\delta| \ll 1. \tag{3.59}$$

Under these approximations, the background evolution (3.25) simplifies to

$$H^2 \simeq \frac{1}{3}V(\phi) \simeq \text{const.} \tag{3.60}$$

which can be used to solve for the expression of the scale factor

$$a(t) \sim e^{Ht}. \tag{3.61}$$

so that the spacetime is approximately *de Sitter*.

Also, the KG/inflaton equation (3.24) becomes

$$3H\dot{\phi} \simeq -V_{,\phi}. \tag{3.62}$$

Furthermore, taking the time-derivative of Eq. (3.62)

$$3\dot{H}\dot{\phi} + 3H\ddot{\phi} = -V_{,\phi\phi}\dot{\phi}, \quad \text{where } V_{,\phi\phi} = \frac{d^2V}{d\phi^2.} \tag{3.63}$$

which leads to

$$\delta + \epsilon_H = -\frac{\ddot{\phi}}{H\dot{\phi}} - \frac{\dot{H}}{H^2} = \frac{1}{3}\frac{V_{,\phi\phi}}{H^2} \simeq \frac{V_{,\phi\phi}}{V}. \tag{3.64}$$

The Hubble slow-roll parameters are approximately related by

$$\epsilon_H \simeq \frac{V_{,\phi}^2}{18H^4} \simeq \frac{1}{2}\left(\frac{V_{,\phi}}{V}\right)^2, \quad \eta_H \simeq 4\epsilon_H - 2\frac{V_{,\phi\phi}}{V}.$$

These can be recast in terms of the *potential slow-roll parameters*,

$$\epsilon_V(\phi) \equiv \frac{m_p^2}{2}\left(\frac{V_{,\phi}}{V}\right)^2, \tag{3.65}$$

$$\eta_V(\phi) \equiv m_p^2\frac{V_{,\phi\phi}}{V}. \tag{3.66}$$

Here, we temporarily reintroduced the Planck mass m_p to make ϵ_V and η_V dimensionless [29].

The number of e-folds before the end of inflation is defined as

$$N(\phi) \equiv \ln\left(\frac{a_{\rm end}}{a}\right) = \int_t^{t_{\rm end}} H\, dt = \int_{\phi_{\rm end}}^{\phi} \frac{H}{\dot{\phi}}\, d\phi \simeq \int_{\phi_{\rm end}}^{\phi} \frac{V}{V_{,\phi}}\, d\phi, \tag{3.67}$$

where the last expression follows from Eqs. (3.60) and (3.62).

Equivalently,

$$N(\phi) = \int_{\phi_{\rm end}}^{\phi} \frac{d\phi}{\sqrt{2\epsilon_H}} \simeq \int_{\phi_{\rm end}}^{\phi} \frac{d\phi}{\sqrt{2\epsilon_V}}. \tag{3.68}$$

To resolve the horizon and flatness problems, the total number of e-folds must exceed approximately 60,

$$N_{\rm tot} \equiv \ln\left(\frac{a_{\rm end}}{a_{\rm start}}\right) \gtrsim 60. \tag{3.69}$$

The precise number depends on the inflationary energy scale and the details of reheating [13, 30].

The fluctuations observed in the Cosmic Microwave Background (CMB) are generated roughly $N_{\rm CMB} \simeq 40$–60 e-folds before the end of inflation [31]. The corresponding field value $\phi_{\rm CMB}$ satisfies

$$\int_{\phi_{\rm end}}^{\phi_{\rm CMB}} \frac{d\phi}{\sqrt{2\epsilon_V}} = N_{\rm CMB} \simeq 40 - 60. \tag{3.70}$$

3.5.2 Power Spectra

Now let us turn over our attention to the power spectra in slow roll inflation. Using Eq. (3.32), the quantity z can be expressed in terms of the first Hubble slow-roll parameter ϵ_H as

$$z = \sqrt{2} m_p \left(a\sqrt{\epsilon_H}\right). \tag{3.71}$$

Next, we calculate the term z''/z appearing in the Mukhanov-Sasaki equation in terms of slow-roll parameters. We start from the relations

$$\epsilon_H = 1 - \frac{\mathcal{H}'}{\mathcal{H}^2}, \qquad \delta = \epsilon_H - \frac{\epsilon_H'}{2\mathcal{H}\epsilon_H}. \tag{3.72}$$

Then z''/z can be written exactly as

$$\frac{z''}{z} = \mathcal{H}^2 \left[2 - \epsilon_H + (\epsilon_H - \delta)(3 - \delta) + \left(\frac{\epsilon_H' - \delta'}{\mathcal{H}} \right) \right]. \tag{3.73}$$

For tensor perturbations, the analogous term is

$$\frac{a''}{a} = \mathcal{H}^2 (2 - \epsilon_H). \tag{3.74}$$

To relate these terms to conformal time τ, we write

$$\tau = -\int \left(\frac{1}{1 - \epsilon_H} \right) d\left(\frac{1}{\mathcal{H}} \right), \tag{3.75}$$

which upon integration by parts and neglecting the second term give

$$\mathcal{H} \simeq -\frac{1}{(1 - \epsilon_H)\tau}. \tag{3.76}$$

Thus, in the leading-order (slow-roll) approximation, the Mukhanov-Sasaki variables become

$$\frac{z''}{z} \simeq \frac{2 + 6\epsilon_H - 3\delta}{\tau^2}, \tag{3.77}$$

$$\frac{a''}{a} \simeq \frac{2 + 3\epsilon_H}{\tau^2}. \tag{3.78}$$

Consequently, the solutions for scalar and tensor modes can be expressed in terms of *Hankel functions* with indices

$$\nu_S \simeq \frac{3}{2} + 2\epsilon_H - \delta, \qquad \nu_T \simeq \frac{3}{2} + \epsilon_H. \tag{3.79}$$

On super-Hubble scales ($-k\tau \to 0$), the scalar and tensor perturbations are given by

$$\mathcal{P}_{\mathcal{R}}(k) = \frac{1}{32\pi^2 m_p^2 \, \epsilon_H} \left[\frac{|\Gamma(\nu_S)|}{\Gamma(3/2)} \right]^2 \left(\frac{k}{a} \right)^2 \left(\frac{-k\tau}{2} \right)^{1 - 2\nu_S}, \tag{3.80a}$$

$$\mathcal{P}_T(k) = \frac{1}{2\pi^2 m_p^2} \left[\frac{|\Gamma(\nu_T)|}{\Gamma(3/2)} \right]^2 \left(\frac{k}{a} \right)^2 \left(\frac{-k\tau}{2} \right)^{1 - 2\nu_T}. \tag{3.80b}$$

Then using Eq. (3.76), the above relations can be written as

$$\mathcal{P}_{\mathcal{R}}(k) = \left(\frac{H^2}{2\pi\dot{\phi}}\right)^2_{k=aH} \left[\frac{|\Gamma(\nu_S)|}{\Gamma(3/2)}\right]^2 2^{2\nu_S-3}(1-\epsilon_H)^{2\nu_S-1}, \tag{3.81a}$$

$$\mathcal{P}_T(k) = \left(\frac{H^2}{2\pi m_p^2}\right)^2_{k=aH} \left[\frac{|\Gamma(\nu_T)|}{\Gamma(3/2)}\right]^2 2^{2\nu_T-3}(1-\epsilon_H)^{2\nu_T-1}. \tag{3.81b}$$

At the leading order in the slow roll parameters, the scalar and tensor spectra reduce to

$$\mathcal{P}_{\mathcal{R}}(k) = \left(\frac{H^2}{2\pi\dot{\phi}}\right)^2_{k=aH}, \tag{3.82a}$$

$$\mathcal{P}_T(k) = \frac{8}{m_p^2}\left(\frac{H}{2\pi}\right)^2_{k=aH}. \tag{3.82b}$$

where the subscript notation indicates that the Hubble parameter H for each mode k should be evaluated at the time of horizon exit for that specific scale [9, 13]. With this, the problem is fully reduced to determining the evolution of the background scalar field and the corresponding Hubble parameter.

The scalar spectral index n_S is defined as

$$n_S - 1 = \left(\frac{d\ln\mathcal{P}_{\mathcal{R}}}{d\ln k}\right)_{k=aH} = \left(\frac{d\ln\mathcal{P}_{\mathcal{R}}}{dt}\right)\left(\frac{dt}{d\ln a}\right)\left(\frac{d\ln a}{d\ln k}\right)_{k=aH}. \tag{3.83}$$

During slow-roll inflation, the Hubble parameter varies very slowly, so we can approximate

$$\left(\frac{d\ln a}{d\ln k}\right)_{k=aH} \simeq 1. \tag{3.84}$$

Thus, the scalar spectral index simplifies to

$$n_S = 1 + \frac{d\ln\mathcal{P}_{\mathcal{R}}}{d\ln k} \simeq 1 + \frac{\dot{\mathcal{P}}_S}{H\mathcal{P}_{\mathcal{R}}}, \tag{3.85}$$

which can be expressed in terms of the slow-roll parameters as

$$n_S \simeq 1 - 4\epsilon_H + 2\delta, \quad n_T \simeq -2\epsilon_H. \tag{3.86}$$

When the slow-roll parameters are small, the resulting power spectrum is nearly scale-invariant [29, 13].

The tensor-to-scalar ratio in the slow-roll limit is given by

$$r \simeq 16\epsilon_H = -8n_T, \tag{3.87}$$

which is commonly referred to as the *consistency relation* [29].

Finally, using Eqs. (3.60),(3.62) and (3.82) the power spectra can be expressed in terms of the inflationary potential $V(\phi)$ in the slow-roll approximation:

$$\mathcal{P}_{\mathcal{R}}(k) \simeq \frac{1}{24\pi^2}\left(\frac{V}{m_p^4}\right)\left(\frac{1}{\epsilon_H}\right)_{k=aH} \simeq \frac{1}{12\pi^2 m_p^6}\left(\frac{V^3}{V_{,\phi}^2}\right)_{k=aH}, \tag{3.88}$$

$$\mathcal{P}_T(k) \simeq \frac{2}{3\pi^2}\left(\frac{V}{m_p^4}\right)_{k=aH}. \tag{3.89}$$

These expressions allow direct comparison of inflationary models with observations [13, 31].

3.6 α-attractor Model

3.6.1 Motivation

The basic idea of the α-attractor theory can be illustrated through a simple toy model with the Lagrangian [32, 33, 34, 35, 36]:

$$\frac{1}{\sqrt{-g}}\mathcal{L} = \frac{R}{2} - \frac{(\partial_\mu\phi)^2}{2(1-\frac{\phi^2}{6\alpha})^2} - V(\phi). \tag{3.90}$$

Here, $\phi(x)$ is the scalar field (inflaton), and the pole in the kinetic term originates from the hyperbolic geometry appearing in supergravity and string theory [35, 36]. The parameter α can take any positive value. Introducing a canonically normalized field φ through $\frac{d\phi}{1-\frac{\phi^2}{6\alpha}} = d\varphi$, one obtains

$$\phi = \sqrt{6\alpha}\tanh\left(\frac{\varphi}{\sqrt{6\alpha}}\right).$$

In terms of the canonical field φ, the theory becomes

$$\frac{1}{\sqrt{-g}}\mathcal{L} = \frac{R}{2} - \frac{(\partial_\mu\varphi)^2}{2} - V\left(\sqrt{6\alpha}\tanh\frac{\varphi}{\sqrt{6\alpha}}\right). \tag{3.91}$$

If the potential $V(\phi)$ and its derivatives are regular at $\phi = \sqrt{6\alpha}$, then for large $\varphi > 0$, the potential behaves as

$$V(\varphi) = V_0 - 2\sqrt{6\alpha}V_0' e^{-\sqrt{\frac{2}{3\alpha}}\varphi}, \tag{3.92}$$

where $V_0 = V(\phi = \sqrt{6\alpha})$ represents the height of the plateau potential, and $V_0' = \partial_\phi V(\phi = \sqrt{6\alpha})$.

The exponential coefficient can be absorbed by redefining (shifting) the field φ, meaning that the inflationary predictions depend only on V_0 and α in the regime $e^{-\sqrt{\frac{2}{3\alpha}}\varphi} \ll 1$ [33, 34].

The amplitude of inflationary perturbations A_s matches the Planck normalization for $\frac{V_0}{\alpha} \sim 10^{-10}$ [31]. For the simplest model $V = \frac{m^2}{2}\phi^2$, belonging to a class of *T-models* with the potential symmetric under $\varphi \to -\varphi$,

$$V(\varphi) = 3m^2 \tanh^2\left(\frac{\varphi}{\sqrt{6\alpha}}\right), \tag{3.93}$$

the condition $\frac{V_0}{\alpha} \sim 10^{-10}$ implies $m \sim 10^{-5}\sqrt{\alpha/6}$ [37].

Different versions of α-attractors approach their universal predictions (3.92) in slightly different ways. For instance, consider the model

$$\frac{1}{\sqrt{-g}}\mathcal{L} = \frac{R}{2} - \frac{3\alpha}{4}\left(\frac{\partial_\mu t}{t}\right)^2 - V(t), \tag{3.94}$$

where the canonical variable φ is related to t through

$$t = e^{-\sqrt{\frac{2}{3\alpha}}\varphi}.$$

Choosing the potential $V(t) = V_0(1-t)^2$ leads to a class of *E-models* with

$$V(\varphi) = V_0\left(1 - e^{-\sqrt{\frac{2}{3\alpha}}\varphi}\right)^2, \tag{3.95}$$

which reproduces the *Starobinsky potential* for $\alpha = 1$ [8].

Notably, the predictions of the E-models (3.95) coincide with those of the T-models (3.93) in the limits $\alpha \to 0$ and $\alpha \to \infty$ [33, 34]. For intermediate values of α, however, the simplest E-models yield slightly larger scalar spectral indices n_S compared to the corresponding T-models [31].

3.6.2 Terminologies

The general forms of the E- and T-model potentials are expressed as

$$V_E(\phi) = V_0 \left(1 - e^{-\lambda_E \frac{\phi}{m_p}}\right)^{2n}, \quad \text{E-model} \tag{3.96a}$$

$$V_T(\phi) = V_0 \tanh^{2n}\left(\lambda_T \frac{\phi}{m_p}\right), \quad \text{T-model} \tag{3.96b}$$

where V_0 denotes the energy scale of inflation, and $n > 0$. λ_E and λ_T are model-dependent parameters.

The initial field value ϕ_{in} is typically taken to coincide with the value of the inflaton at the end of inflation, ϕ_{end}. This point is determined by the condition that the first potential slow-roll parameter,

$$\epsilon_V = \frac{m_p^2}{2}\left(\frac{V_{,\phi}}{V}\right)^2, \tag{3.97}$$

reaches unity, i.e. $\epsilon_V(\phi_{\text{end}}) = 1$.

Applying Eq. (3.97) to the E- and T-model potentials in Eq. (3.96), we obtain the analytic expressions for the field value at the end of inflation:

$$\phi_{\text{end}} = \begin{cases} \dfrac{m_p}{\lambda_E} \ln\left(1 + \frac{1}{\sqrt{2}} p \lambda_E\right), & \text{E-model,} \\ \dfrac{m_p}{2\lambda_T} \operatorname{arcsinh}(\sqrt{2} p \lambda_T), & \text{T-model.} \end{cases} \tag{3.98}$$

where $p = 2n$. In the limit,

$$\lambda \phi_* / m_p \geq 1 \tag{3.99}$$

where ϕ_* denotes the value of the inflaton field when the pivot scale exits the Hubble radius, the predictions of these models become

$$n_S \simeq 1 - \frac{2}{N_*}, \qquad r \simeq \frac{2}{\lambda_E^2 N_*^2}, \quad \text{E-model,} \tag{3.100a}$$

$$n_S \simeq 1 - \frac{2}{N_*}, \qquad r \simeq \frac{8}{\lambda_T^2 N_*^2}. \quad \text{T-model.} \tag{3.100b}$$

Here, N_* represents the number of e folds remaining until the end of inflation at the pivot scale.

It's evident that these predictions are independent of n. Due to this property, these models are called *cosmological attractors* [35, 34].

Chapter 4

Simulations and Results

4.1 Numerical analysis of background dynamics

A comprehensive understanding of the inflationary background dynamics can be achieved by studying the time evolution of the scalar field ϕ, its time derivative $\dot{\phi}$, and the Hubble parameter H. The scale factor a evolves directly according to the relation $H = \dot{a}/a$. The full dynamical system, expressed as a function of cosmic time t, is given by

$$H^2 = \frac{1}{3m_p^2}\left(\frac{1}{2}\dot{\phi}^2 + V(\phi)\right), \tag{4.1}$$

$$\dot{H} = -\frac{\dot{\phi}^2}{2m_p^2}, \tag{4.2}$$

$$\ddot{\phi} = -3H\dot{\phi} - V_{,\phi}(\phi), \tag{4.3}$$

where the specific form of the potential $V(\phi)$ depends on the inflationary model considered, though the numerical algorithm itself remains largely model-independent. We can re-write the potential as

$$V(\phi) = V_0 f(\phi) \tag{4.4}$$

For numerical simulations, it is convenient to express these equations in terms of dimensionless quantities, which eliminates the need to track units explicitly. Additionally, the time variable is rescaled by a constant factor S, chosen appropriately based on the energy scale of the system[1]. The dimensionless variables

[1]Depending upon the potential, we usually choose the value of S to be in the range $S \in [10^{-5}, 10^{-3}]$.

are defined as [38]

$$T = \frac{tm_p}{S}, \tag{4.5}$$

$$x = \frac{\phi}{m_p}, \tag{4.6}$$

$$y = \frac{\dot{\phi}}{m_p^2}\frac{1}{S}, \tag{4.7}$$

$$z = \frac{H}{m_p}\frac{1}{S}, \tag{4.8}$$

$$A = \frac{am_p}{S}. \tag{4.9}$$

In terms of these dimensionless variables, the corresponding dynamical equations governing the evolution of the system are expressed as [38]

$$\frac{dx}{dT} = y, \tag{4.10}$$

$$\frac{dy}{dT} = -3zy - \frac{v_0}{S^2}f_{,x}(x), \tag{4.11}$$

$$\frac{dz}{dT} = -\frac{1}{2}y^2, \tag{4.12}$$

$$\frac{dA}{dT} = Az. \tag{4.13}$$

We can also define the dimensionless potential to be [38]

$$\frac{V(\phi)}{m_p^4} \equiv \frac{V_0}{m_p^4}f(\phi) = v_0 f(\phi) \tag{4.14}$$

We solve the above system of dynamical equations using appropriate initial conditions. In this analysis, the `solve_ivp` function from the `scipy.integrate` package is utilized to perform numerical integration. By specifying the initial conditions $\{x_i, y_i, z_i, A_i\}$ for the primary dynamical variables $\{x, y, z, A\}$, we compute their time evolution during inflation. The corresponding derived (dimensionless) dynamical quantities are then obtained from these primary variables

as follows:

$$N = \ln \frac{A}{A_i}, \tag{4.15a}$$

$$\epsilon_H = \frac{1}{2}\frac{y^2}{z^2}, \quad \eta_H = -\frac{1}{yz}\frac{dy}{dT}, \tag{4.15b}$$

$$P_s = \frac{1}{8\pi^2}\frac{(Sz)^2}{\epsilon_H}, \quad P_t = \frac{2}{\pi^2}(Sz)^2, \tag{4.15c}$$

$$n_S = 1 + 2\eta_H - 4\epsilon_H, \quad n_T = -2\epsilon_H, \tag{4.15d}$$

$$r = 16\epsilon_H. \tag{4.15e}$$

The last three equations above are valid under the slow-roll approximation.

We define N_T as the total number of e-folds of accelerated expansion that occur between an arbitrary initial time and the end of inflation, where the latter is characterized by $\epsilon_H = 1$. It is often convenient to introduce another variable, $N_e = N_T - N$, which represents the instantaneous number of e-folds remaining before the end of inflation.

By definition, $N_e = 0$ at the end of inflation, while $N_e > 0$ corresponds to earlier epochs. This variable serves as our primary time parameter for plotting the evolution of various inflationary observables. To achieve sufficient inflation, i.e. $N_T > 60$, the initial value of the inflaton field must be sufficiently large, though this requirement depends on the specific inflationary model.

The initial value of the scale factor, A_i, can be chosen arbitrarily in a spatially flat universe. However, depending on the energy scale of inflation, one may assign an appropriate value. In this work, we adopt a representative value of $A_i = 1 \times 10^{-3}$, though its precise choice has negligible impact on the overall dynamics.

For the initial inflaton field value x_i, it is necessary to ensure that it is sufficiently large (or sufficiently small in the case of symmetry-breaking hilltop potentials) to generate an adequate amount of inflation, typically $N_T \geq 60$.

To determine the appropriate x_i, we employ the `brentq` root-finding algorithm, which combines root bracketing, interval bisection, and inverse quadratic interpolation, to solve for x_i from the integrand of N corresponding to a specified total number of e-folds, $N_T = 77.4859$.

The potential normalization parameter, v_0, is also determined using the same method to reproduce the CMB-normalized scalar power spectrum (Eq. 4.15c) at the pivot scale $N_* = 60$, where $P_{S*} = 2.1 \times 10^{-9}$.

Observations from several Cosmic Microwave Background (CMB) experiments, including the *Planck* mission [1] and the BICEP/Keck collaboration, have placed stringent constraints on the properties of primordial fluctuations. In particular, the latest *Planck* 2018 data [31] constrain the amplitude of scalar perturbations at the CMB pivot scale $k_* = 0.05\ \mathrm{Mpc}^{-1}$ to be

$$P_s = 2.1 \times 10^{-9}. \tag{4.16}$$

The corresponding 2σ constraint on the scalar spectral index is

$$n_S \in [0.957,\, 0.976]. \tag{4.17}$$

Furthermore, the combined analysis of *Planck* 2018 [31] and BICEP/Keck [2] data provides an upper bound on the tensor-to-scalar [39],

$$r \leq 0.036, \tag{4.18}$$

which corresponds to an upper limit on the tensor amplitude

$$P_t \leq 3.6 \times 10^{-2} A_S. \tag{4.19}$$

These observational bounds impose a constraint on the inflationary Hubble scale,

$$H_{\mathsf{inf}} \leq 4.7 \times 10^{13}\ \mathrm{GeV}. \tag{4.20}$$

Using the CMB upper limit on r together with Eqs. (3.86), (3.87) and (4.18), we can further impose bounds on the slow-roll parameters [40]:

$$\epsilon_H \leq 0.00225, \tag{4.21a}$$
$$|n_T| \leq 0.0045, \tag{4.21b}$$
$$|\eta_H| \in [0.0075,\, 0.0215]. \tag{4.21c}$$

4.2 Numerical analysis for quantum fluctuations

In the previous section, we employed the slow-roll approximation to derive analytical expressions for the inflationary power spectra in terms of background quantities such as H, ϵ_H, and η_H. Thus, it was sufficient to simulate only the background dynamics for a given potential to evaluate the relevant inflationary observables. However, in scenarios where one or both of the slow-roll conditions (3.59) are violated, a more precise treatment requires numerically solving

the Mukhanov–Sasaki equation (3.34 & 3.41) for each comoving wavenumber k.

To facilitate this, we first express the Mukhanov–Sasaki equation in cosmic time as

$$\frac{d^2v_k}{dt^2} + H\frac{dv_k}{dt} + \left(\frac{k^2}{a^2} - \frac{1}{a^2}\frac{z''}{z}\right) v_k = 0. \tag{4.22}$$

Here, z is not the dimensionless Hubble parameter introduced in the previous section, but rather the quantity defined in the Mukhanov–Sasaki formalism as $z = aM_P\sqrt{2\epsilon_H}$. The effective mass term z''/z in Eq. (4.22) can be written as

$$\frac{z''}{z} = a^2\left[\frac{5}{2}\frac{\dot\phi^2}{M_P^2} + 2\frac{\dot\phi\ddot\phi}{HM_P^2} + 2H^2 + \frac{1}{2}\frac{\dot\phi^4}{H^2M_P^4} - V_{,\phi\phi}(\phi)\right]. \tag{4.23}$$

Since v_k is complex-valued, it is numerically convenient to decompose it into its real and imaginary components, each evolving according to the same differential equation but initialized with the real and imaginary parts of the Bunch–Davies vacuum (3.54).

In terms of our dimensionless variables, the Mukhanov–Sasaki equation for scalar perturbations takes the form

$$\frac{d^2v_k}{dT^2} + z\frac{dv_k}{dT} + \left[\frac{k^2}{A^2} - \frac{5}{2}y^2 + 2\frac{y}{z}\left(3zy + \frac{v_0}{S^2}f_{,x}\right) - 2z^2 - \frac{1}{2}\frac{y^4}{z^2} + \frac{v_0}{S^2}f_{,xx}\right] v_k = 0. \tag{4.24}$$

Our primary objective in this section is to numerically solve Eq. (4.24) for the Fourier modes v_k corresponding to each comoving wavenumber k, and to obtain the frozen value of the scalar power spectrum of $\mathcal{P}_\mathcal{R}$ given by Eq. (3.88) once the mode becomes super-Hubble. The relation between a comoving scale k and its Hubble-exit epoch is given by $k = aH$. Since we are only interested in the super-Hubble power spectra, it suffices to evolve v_k for a limited period around the Hubble-exit of the corresponding scale.

In the same manner, we can obtain the corresponding Mukhanov–Sasaki equation for tensor perturbations (at linear order in perturbation theory) in dimensionless form as

$$\frac{d^2h_k}{dT^2} + z\frac{dh_k}{dT} + \left[\frac{k^2}{A^2} + \frac{1}{2}y^2 - 2z^2\right] h_k = 0. \tag{4.25}$$

We explicitly express the Mukhanov–Sasaki equations for scalar and tensor fluctuations in terms of dimensionless variables (as employed in our numerical code)

as follows:

$$v_{k,T} = \frac{dv_k}{dT}, \tag{4.26}$$

$$\frac{dv_{k,T}}{dT} = -z\, v_{k,T} - \left[\frac{k^2}{A^2} - \frac{5}{2}y^2 + 2\frac{y}{z}\left(3zy + \frac{v_0}{S^2}f_{,x}\right) - 2z^2 - \frac{1}{2}\frac{y^4}{z^2} + \frac{v_0}{S^2}f_{,xx}\right] v_k, \tag{4.27}$$

$$h_{k,T} = \frac{dh_k}{dT}, \tag{4.28}$$

$$\frac{dh_{k,T}}{dT} = -z\, h_{k,T} - \left[\frac{k^2}{A^2} + \frac{1}{2}y^2 - 2z^2\right] h_k. \tag{4.29}$$

In our numerical setup, both v_k and h_k are decomposed into their real and imaginary components, which are then evolved independently under the corresponding Bunch–Davies initial conditions.

We next proceed to identify the different comoving scales k by determining their respective Hubble-exit epochs. This can be achieved by plotting aH (in logarithmic scale) as a function of N_e, and identifying the value of aH at $N_e = N_*$ as the CMB pivot scale k_p. Throughout our analysis, we take $N_* = 60$. In this way, each comoving scale k can be associated with a specific value of N_e corresponding to its Hubble-exit epoch. This establishes a one-to-one correspondence between k and N_e, allowing us to use them interchangeably in subsequent analysis.

We impose the Bunch–Davies initial conditions for each mode v_k at an epoch when it is well inside the Hubble radius, i.e., when the mode is sub-Hubble. In practice, for most inflationary potentials, the Bunch–Davies conditions can be safely applied as long as $k \geq 100\, aH$.

Consequently, instead of integrating the Mukhanov–Sasaki equation for each mode from the beginning of inflation (starting from $\phi_i > \phi_*$), we initialize the mode about five e-folds before its Hubble-exit epoch. This optimization significantly reduces the computational time required for the simulations.

At this initial epoch, the scale factor is taken as $A_i \exp(N_T - N_e - 5)$, while the field variables $\{x_i, y_i\}$ are initialized using the corresponding background solutions $\{x, y, z, A\}$. The mode function v_k and its derivative $\dot{v}_k$ are then initialized with the Bunch–Davies vacuum conditions.

We numerically evolve the full set of equations from $T = T_i$ to $T = T_f$ until the mode becomes super-Hubble and the corresponding power spectrum, $k^3|\mathcal{R}|^2/2\pi^2$ reaches a constant ("frozen") value. This typically occurs within about five e-folds after Hubble-exit for the class of inflationary models considered here. The frozen value is recorded as the scalar power spectrum for that mode.

The same procedure is repeated for multiple modes, each characterized by a

different Hubble-exit epoch N_e, until we obtain the super-Hubble power spectra across the range of comoving scales of interest.

4.3 E-model potential

4.3.1 Case: n=1

For $n = 1$, the E-model potential becomes

$$V(\phi) = V_0 \left(1 - e^{-\lambda_E \frac{\phi}{mp}}\right)^2 \tag{4.30}$$

which resembles the *Starobinsky potential* for $\lambda_E = \sqrt{2/3}$. I am taking the same value for λ throughtout this section.

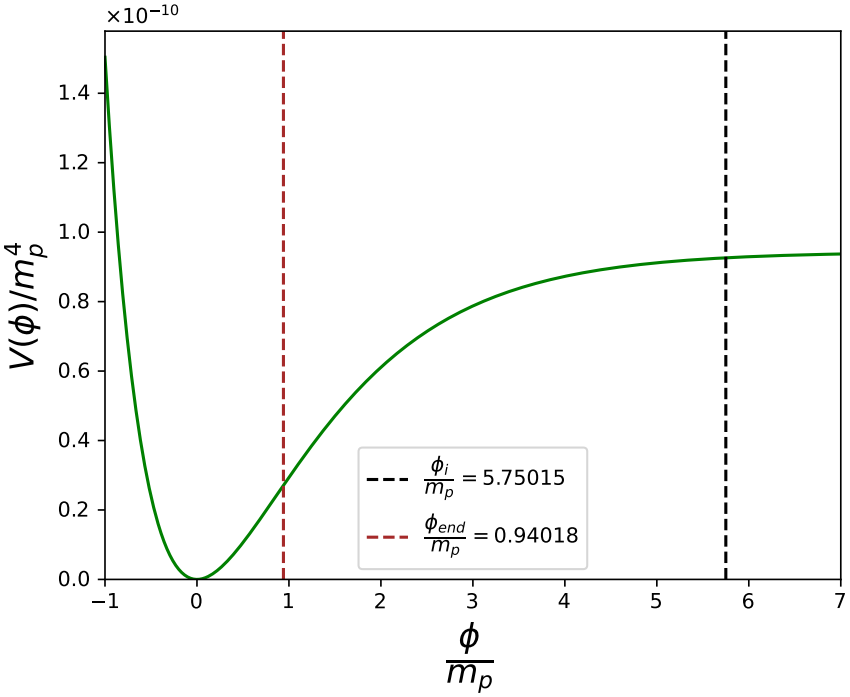

Figure 4.1: E-model potential for $n = 1$. The start and end of inflation are denoted by black and red dotted line, respectively.

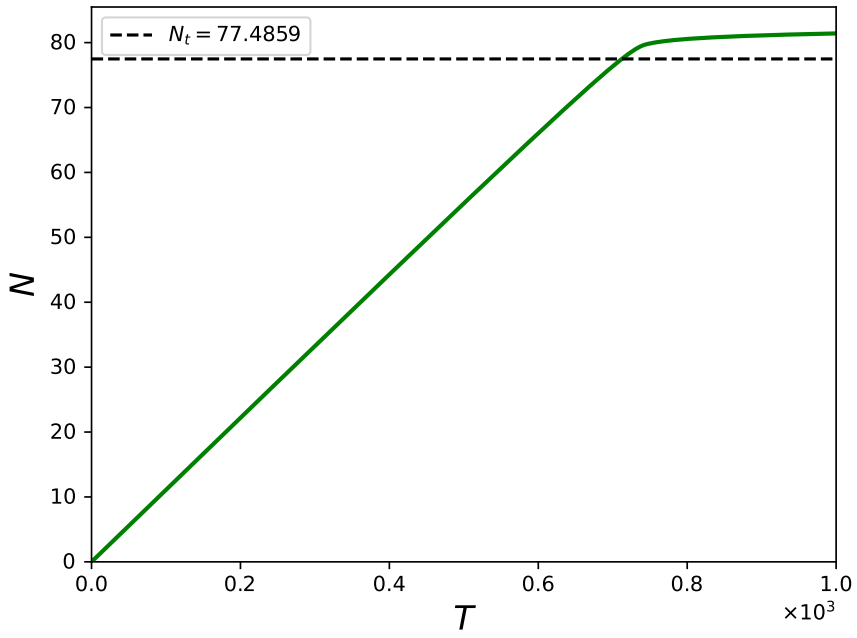

Figure 4.2: Time evolution of the number of e-folds of expansion of the universe is shown for Starobinsky potential. At the end of inflation i.e. $Nt = 77.4859$, the expansion becomes constant which denotes the end of inflation.

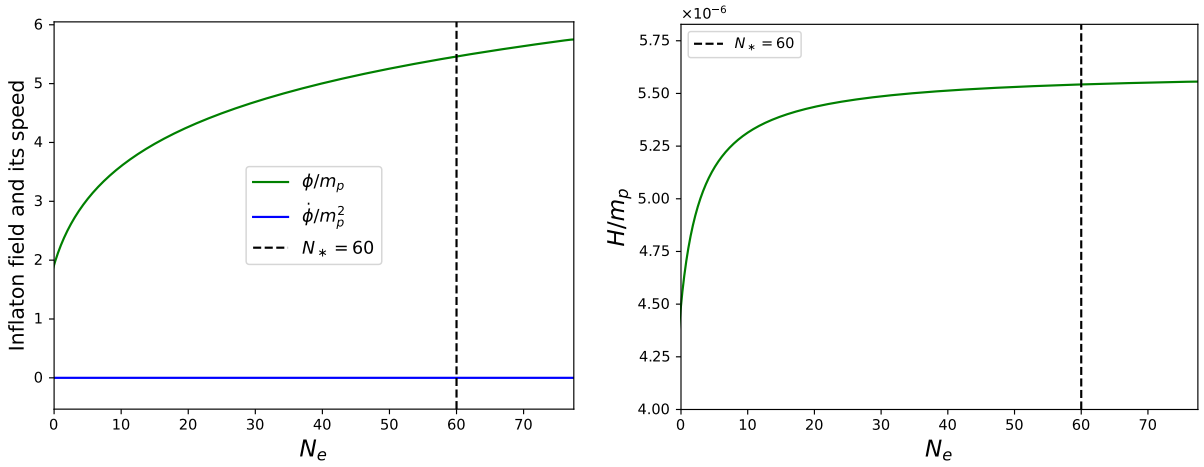

(a) (b)

Figure 4.3: (a) Evolution of inflaton field ϕ, and its speed $\dot{\phi}$. (b) Evolution of Hubble parameter. Note that during slow-roll inflation, $\dot{\phi}$ and H are nearly constant, while ϕ changes quite slowly. However, ϕ and H begin to change rapidly towards the end of inflation.

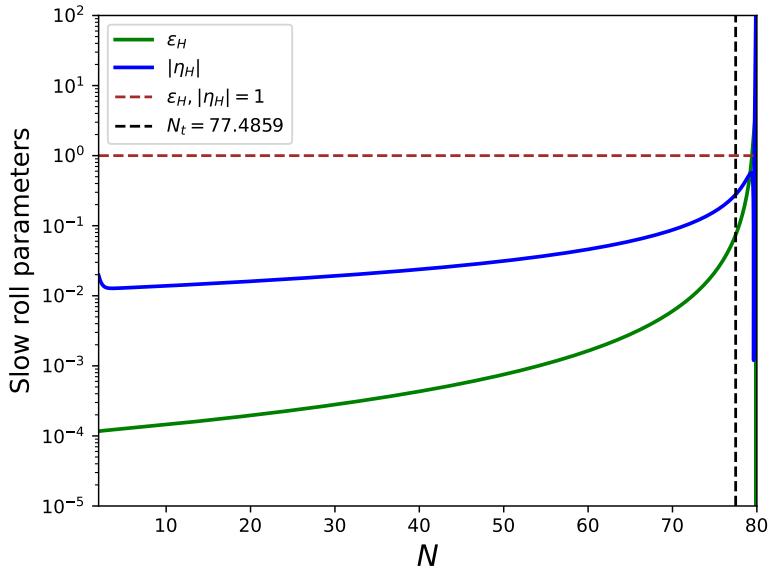

Figure 4.4: Evolution of the slow-roll parameters ϵ_H and $|\eta_H|$ is shown as a function of the number of e-folds. Before the end of inflation i.e. $N = 77.4859$, the slow-roll conditions are satisfied i.e. $\epsilon_H, |\eta_H| \ll 1$.

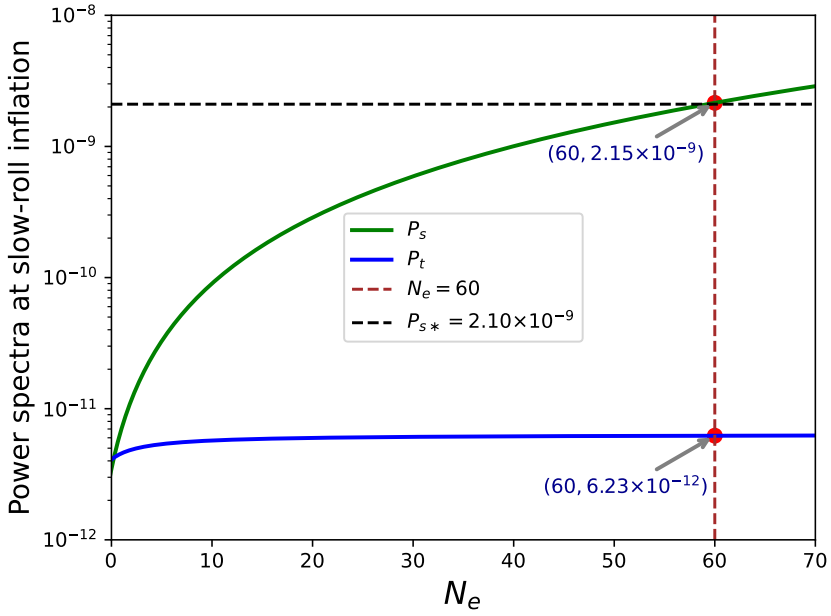

Figure 4.5: The power spectra of scalar and tensor quantum fluctuations are shown for comoving modes exiting the Hubble radius at different N_e values before the end of inflation for Starobinsky potential. At CMB window i.e. $N_e = 60$, the scalar power spectra value closely matches with that of our pivot scale.

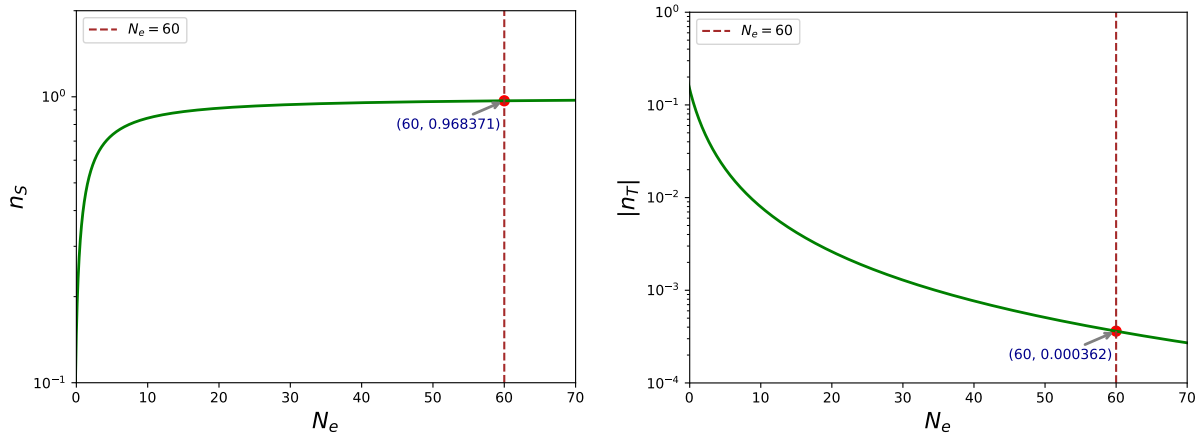

(a) (b)

Figure 4.6: The scalar and tensor spectral indices n_S (a) and $|n_T|$ (b) are shown as a function of N_e for Starobinsky potential. Around the pivot scale, they take the approximate values $n_S \simeq 0.968$ and $n_T \simeq -0.0004$. These fall within the CMB constraints mentioned in (4.17) and (4.21b).

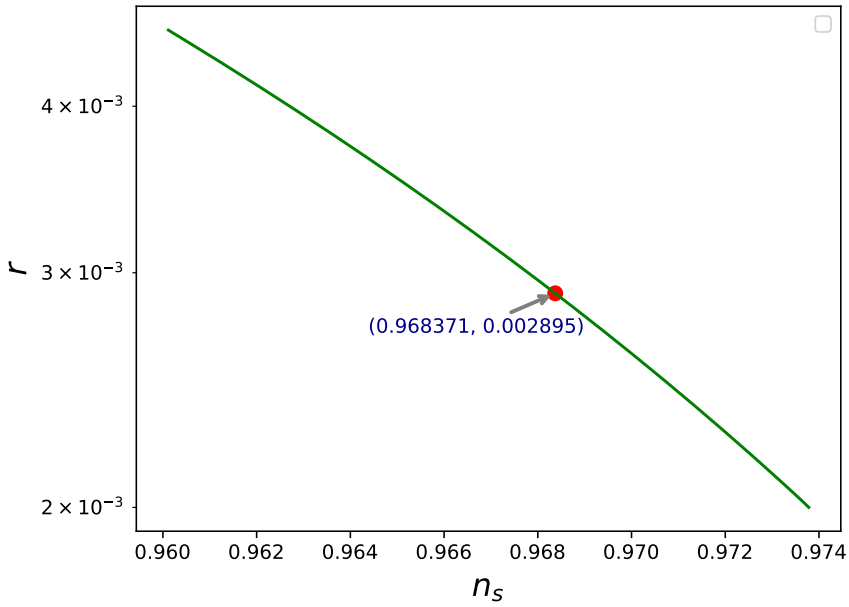

Figure 4.7: The tensor-to-scalar ratio of the Starobinsky potential are shown for different scalar spectral indices. This figure shows the path taken by the model along the $n_S - r$ plot. At the CMB scale, the value of r is found to be $\simeq 0.003$ which is well within the bound (4.18).

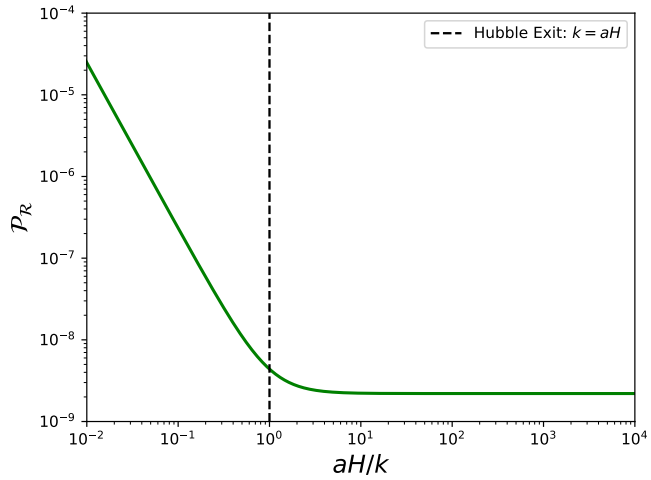

Figure 4.8: Evolution of the scalar power spectrum $\mathcal{P}_\mathcal{R}$ obtained by numerically solving the Mukhanov–Sasaki equation for a mode exiting the Hubble radius about 60 e-folds before the end of inflation (Starobinsky potential). The power decreases as $\mathcal{P}_\mathcal{R} \propto (aH)^{-2}$ in the sub-Hubble regime ($k \gg aH$) and freezes to a constant after Hubble exit ($k \ll aH$), representing the super-Hubble power for that mode. Repeating this for different k yields the full scalar power spectrum.

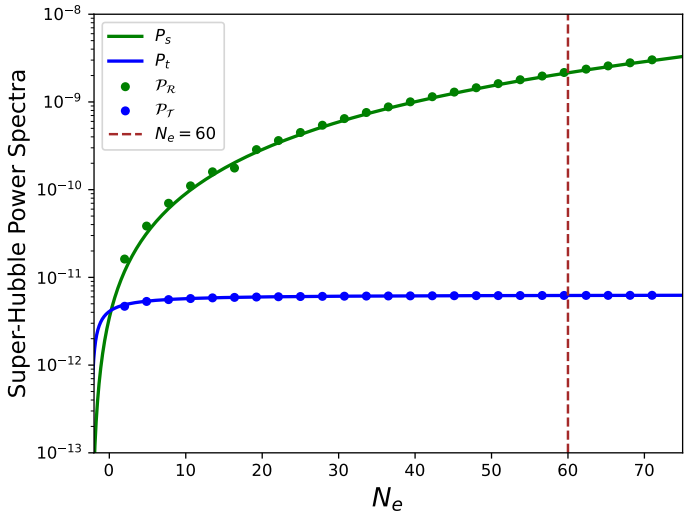

Figure 4.9: Comparison of the super-Hubble power spectra of scalar (green) and tensor (blue) fluctuations for modes exiting the Hubble radius at different N_e before the end of inflation, for the Starobinsky potential (Eq. 4.30). The solid lines denote spectra computed under the slow-roll approximation (Eq. 4.15c), while the scattered points represent results from numerical solutions of the Mukhanov–Sasaki equation (Eqs. 4.27, 4.29). For the Starobinsky model, the slow-roll and numerical spectra show excellent agreement.

4.3.2 Comparison between different n-valued potentials

Let's plot the E-model potentials for $n = 1, 2, 3$ and see how the the parameters vary from each other.

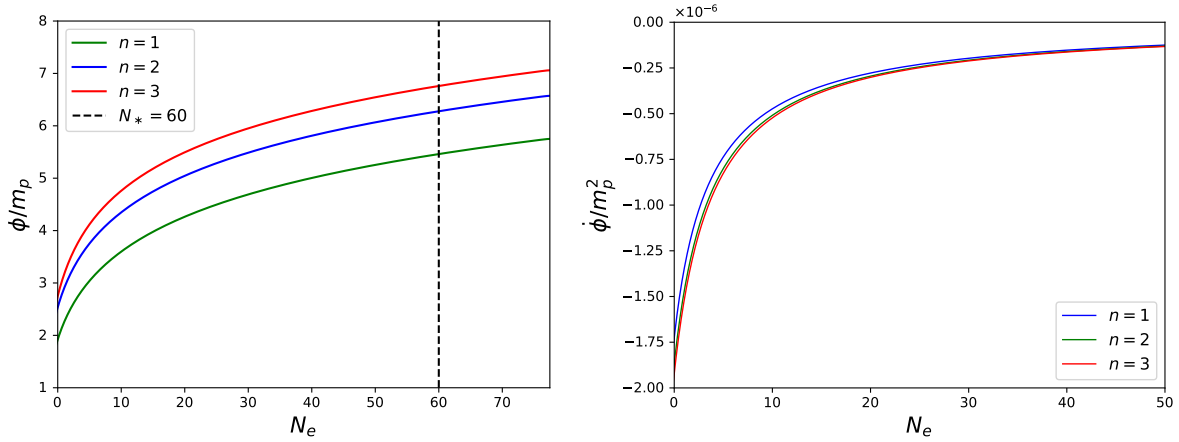

(a) (b)

Figure 4.10: (a) Evolution of inflaton field ϕ, and (b) its speed $\dot{\phi}$. During slow-roll inflation, although $\dot{\phi}$ traverses different trajectory, they seem to converge at the end of inflation. However, $\dot{\phi}$ does not seem to diverge that much while changing the value of n.

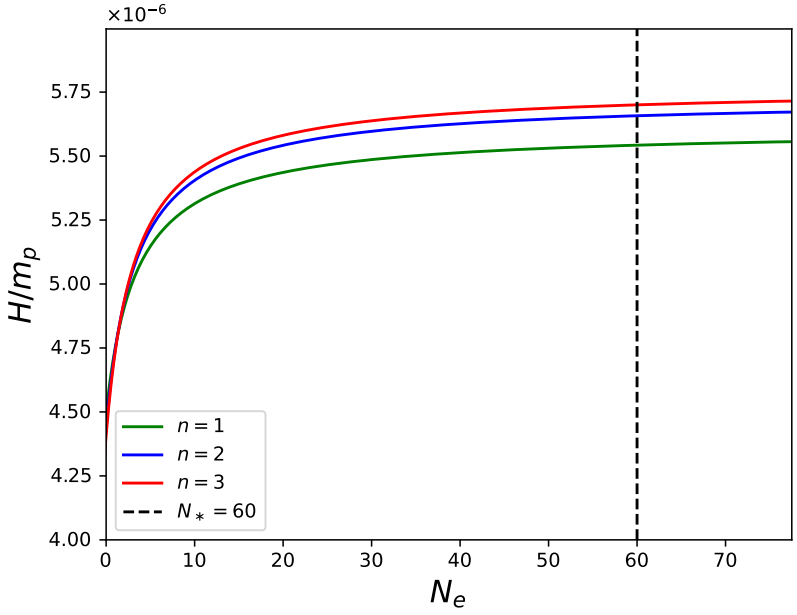

Figure 4.11: Evolution of Hubble parameter. The trajectories seems to follow that for ϕ but they diverge less for different n-models.

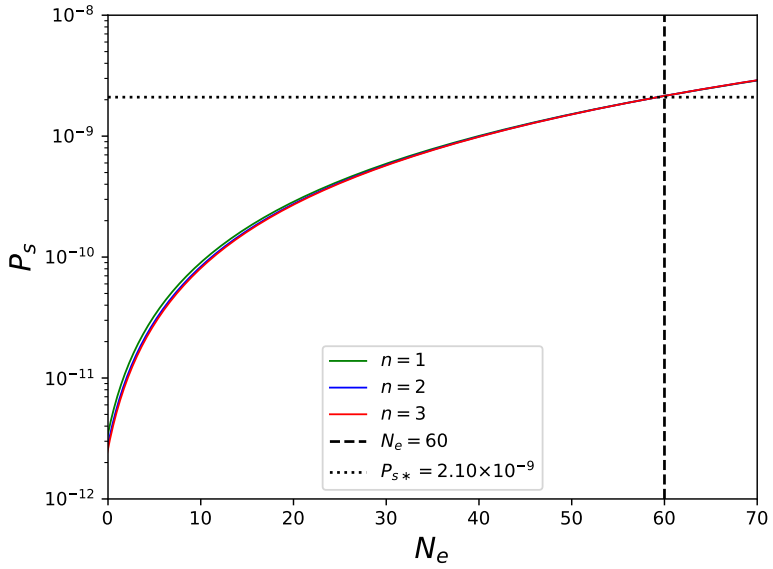

Figure 4.12: Scalar power spectra for quantum fluctuations plotted for comoving modes exiting the Hubble radius at different N_e values before the end of inflation for $n = 1, 2, 3$ valued E-potential. The differences are not that much visible. At CMB window i.e. $N_e = 60$, the scalar power spectra values closely match with that of our pivot scale.

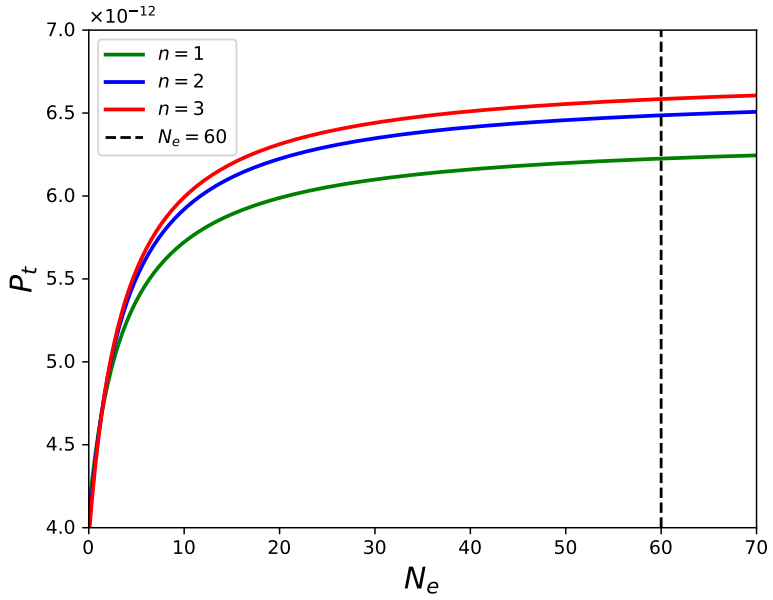

Figure 4.13: Power spectra of tensor quantum fluctuations for comoving modes exiting the Hubble radius at different N_e values before the end of inflation for E-potential at different n values. Unlike P_S, the curves are distinct but they do converge at the end of inflation.

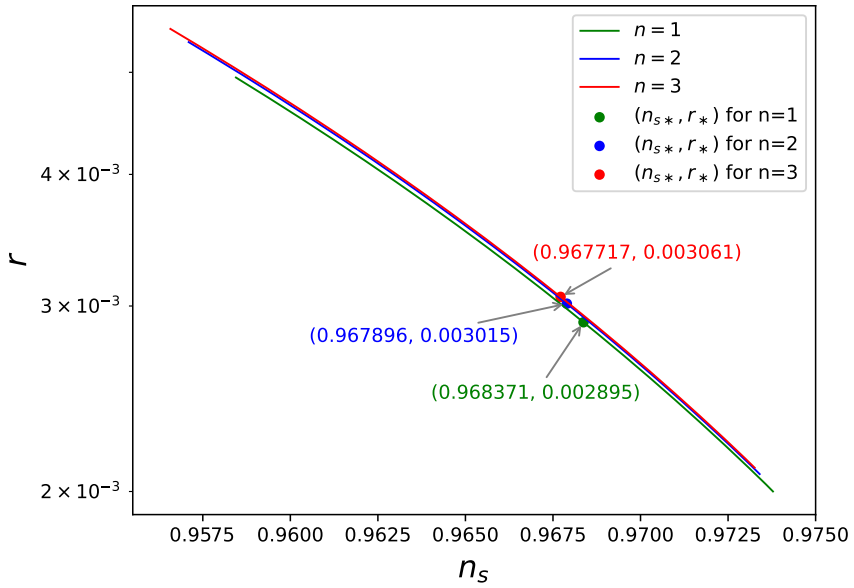

Figure 4.14: The tensor-to-scalar ratio of three different n-valued E-potentials are shown for different scalar spectral indices. At the CMB scale, the values of r seem to be increasing with the value of n but still are very close to one another and well within the bound (4.18).

4.4 T-model potential

4.4.1 Case: Small-field limit

The T-model for $n = 1$ is just as follows

$$V(\phi) = V_0 \tanh^2\left(\lambda_T \frac{\phi}{m_p}\right) \tag{4.31}$$

In case of small $\lambda_T \ll 1$, $\tanh\left(\lambda_T \frac{\phi}{m_p}\right) \simeq \lambda_T \frac{\phi}{m_p}$ and the expression becomes that of a *quadratic potential*.

$$V(\phi) \simeq V_0^2 \lambda_T^2 \left(\frac{\phi}{m_p}\right)^2 = \frac{1}{2} m^2 \phi^2, \qquad \text{where } m = \frac{\sqrt{2} V_0 \lambda_T}{m_p}. \tag{4.32}$$

For converging into quadratic potential, I am taking an arbitrary small value for $\lambda_T = 10^{-4}$.

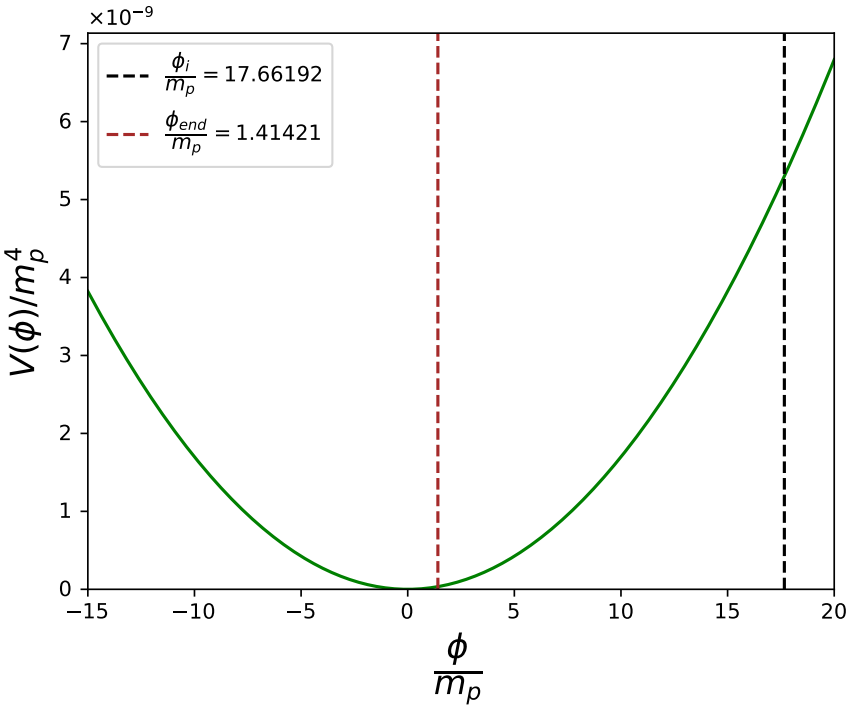

Figure 4.15: T-model potential for $n = 1, \lambda_T \ll 0$ which resembles the quadratic potential. The initial and final points of inflation are marked by the black and red dashed lines, respectively.

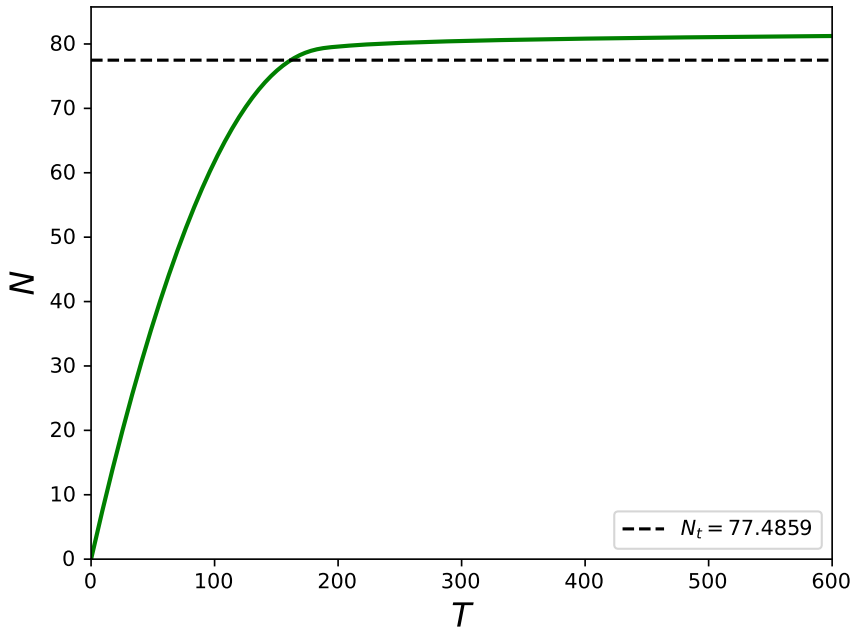

Figure 4.16: Time evolution of the number of T-folds for the quadratic model. The value $N_t = 77.4859$ marks the point where inflation ends and the expansion rate stops accelerating.

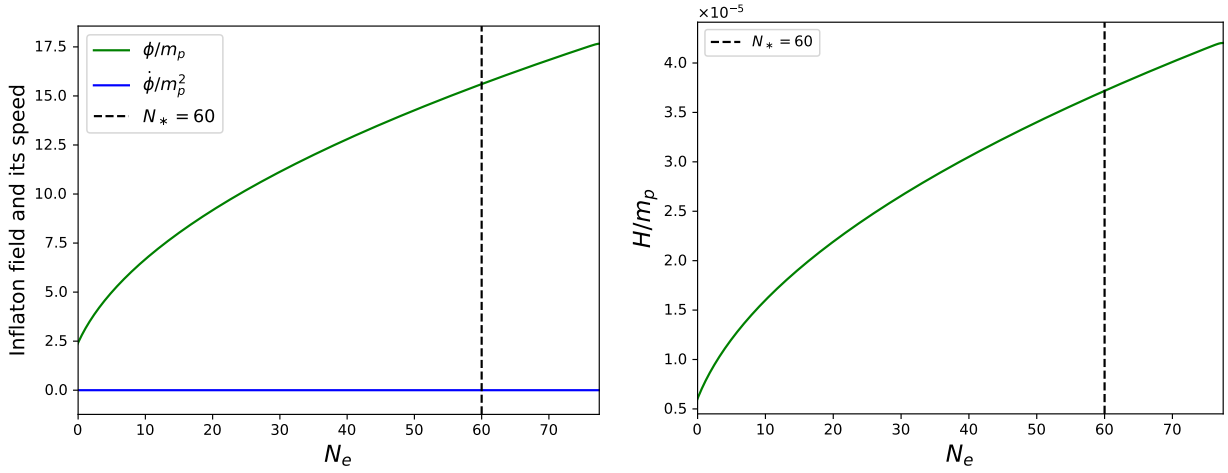

(a) (b)

Figure 4.17: (a) Evolution of the inflaton field ϕ and its velocity $\dot{\phi}$. (b) Behavior of the Hubble parameter H. During slow-roll inflation, only $\dot{\phi}$ remains nearly constant. While both ϕ and H change only gradually, they vary more rapidly near the end of inflation.

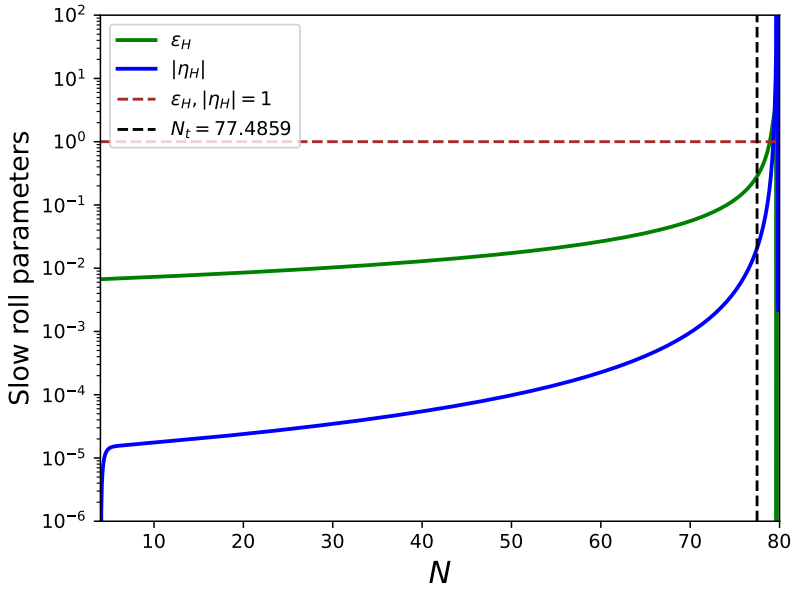

Figure 4.18: Evolution of the slow-roll parameters ϵ_H and $|\eta_H|$ as functions of the number of e-folds. For most of the inflationary period up to $N = 77.4859$, both parameters remain much smaller than unity, indicating valid slow-roll conditions.

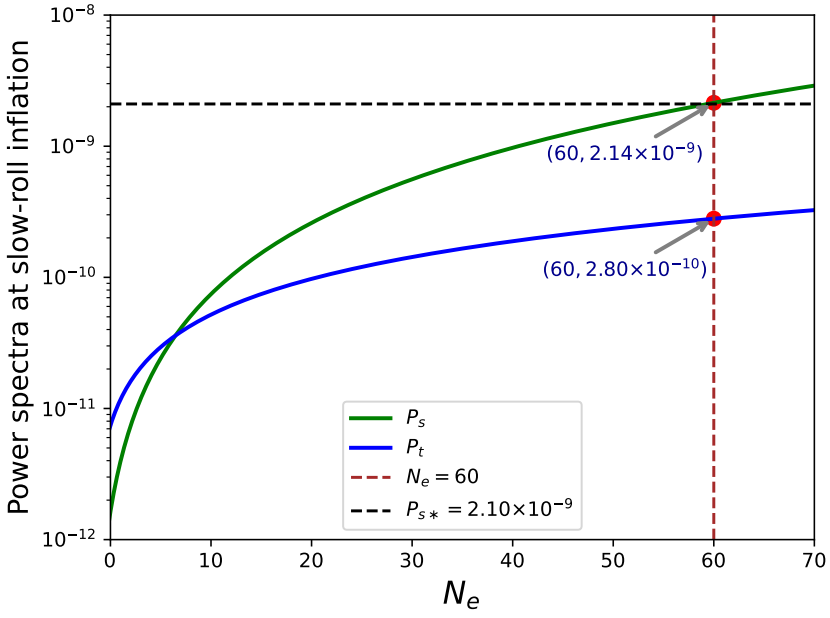

Figure 4.19: Scalar and tensor power spectra for modes exiting the Hubble radius at various N_e values for the quadratic model. At $N_e = 60$, corresponding to the CMB scale, the scalar amplitude agrees well with the pivot-scale value.

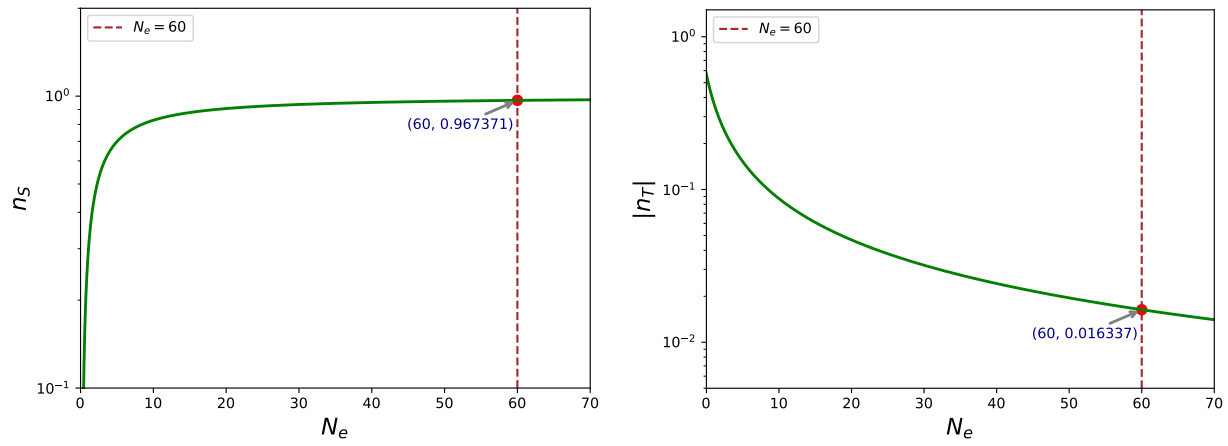

(a) (b)

Figure 4.20: (a) Scalar spectral index n_S and (b) tensor spectral index $|n_T|$ as functions of N_e for the quadratic model. Near the pivot scale, the values are approximately $n_S \simeq 0.967$ and $n_T \simeq -0.0163$. While value of n_S is consistent with Eq. (4.17), n_T is not bounded by Eq. (4.21b).

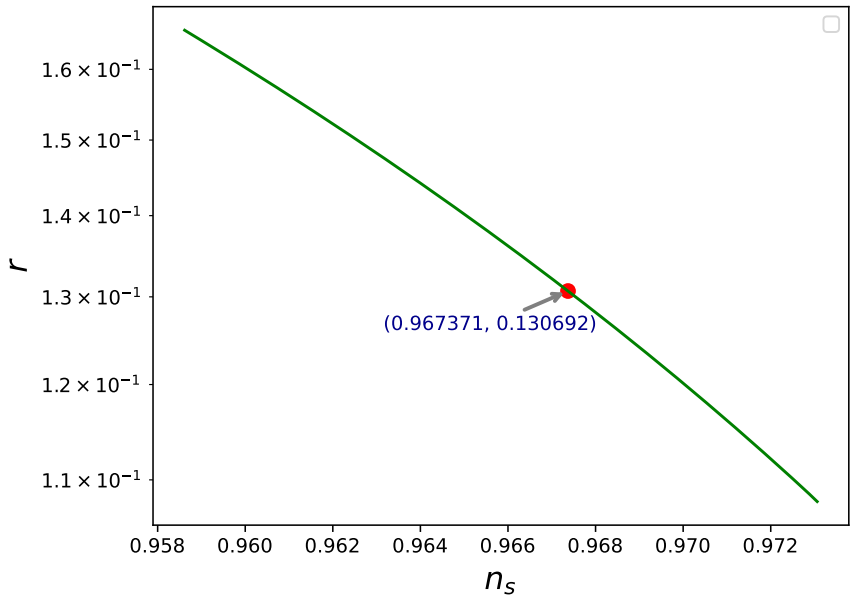

Figure 4.21: Tensor-to-scalar ratio r for the quadratic model shown as a function of the scalar spectral index n_S which illustrates the trajectory of the quadratic model. At the CMB pivot scale, $r \simeq 0.13$ has exceeded the limit given in (4.18).

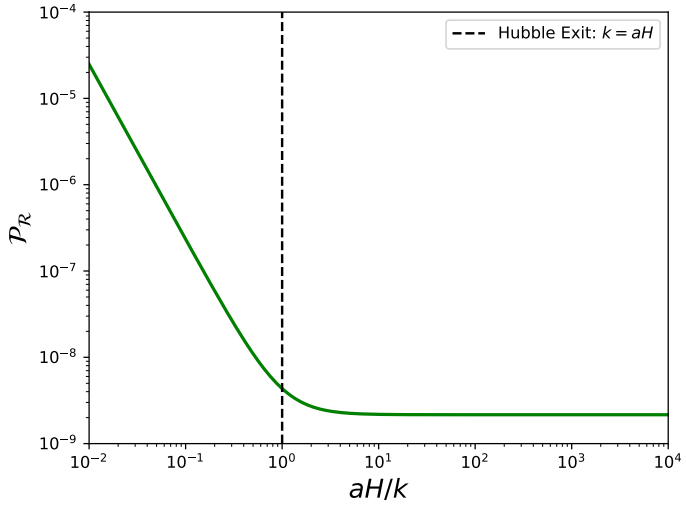

Figure 4.22: Scalar power spectrum $\mathcal{P}_\mathcal{R}$ obtained by solving the Mukhanov–Sasaki equation for a mode exiting the Hubble radius around 60 e-folds before the end of inflation (Quadratic potential model). The usual $(aH)^{-2}$ decay in the sub-Hubble regime ($k \gg aH$) and subsequent freezing on super-Hubble scales ($k \ll aH$) are clearly visible.

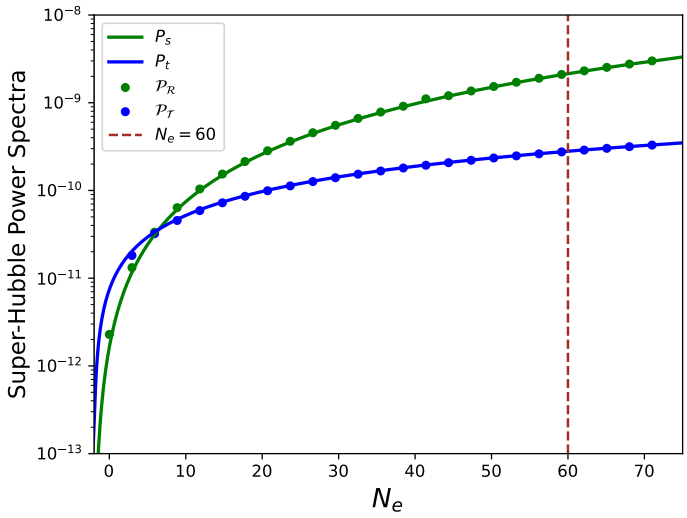

Figure 4.23: Comparison of the super-Hubble scalar (green) and tensor (blue) power spectra for modes leaving the Hubble radius at different N_e for the quadratic potential model (Eq. 4.32). Solid curves denote slow-roll predictions (Eq. 4.15c), while scattered points show numerical solutions of the Mukhanov–Sasaki equations (Eqs. 4.27, 4.29). The close match demonstrates the accuracy of the slow-roll approximation for this model.

In case of quadratic potential, the main reason for violating CMB constraints on n_T (4.21b) and r (4.18) is the minuscule value of λ_T which breaks the condition (3.99) for α-attractor CMB predictions.

The simple quadratic inflationary model (4.32) predicts a tensor-to-scalar ratio $r \approx 8/N$, giving $r \sim 0.13$, and a tensor spectral index $n_T = -r/8 \sim -0.016$ for $N \sim 60$. Therefore, the quadratic potential is in significant tension with current data disfavoring BICEP/Keck 2018 and Planck Public Release 4 [31, 39].

4.4.2 Comparison between different n-valued potentials

Let's plot the T-model potentials for $n = 1, 2, 3$ and see how the results differ. Here, I take a larger value $\lambda = 0.5$ for demonstrating genuine T-model attractors.

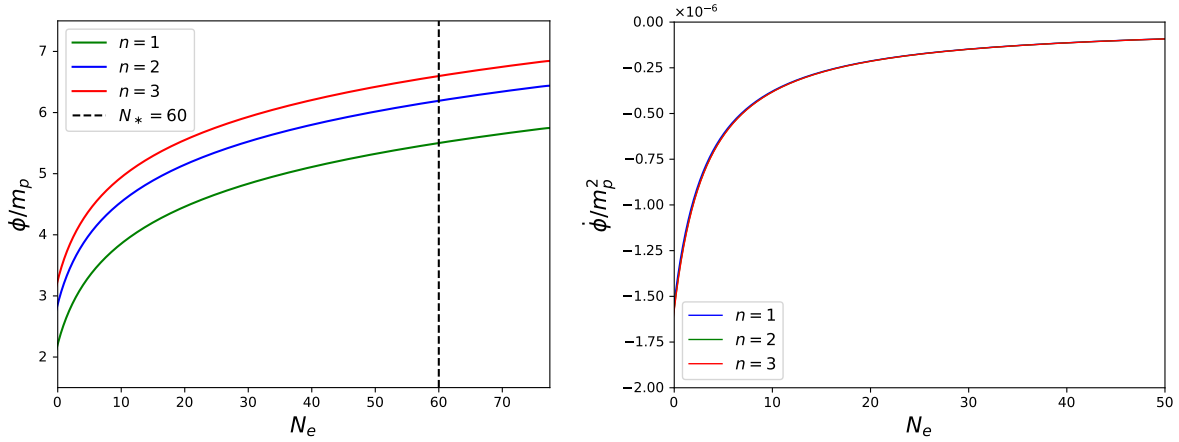

(a) (b)

Figure 4.24: Behaviour of (a) the inflaton field ϕ and (b) its velocity $\dot{\phi}$. Although ϕ follows distinct paths during slow-roll inflation, the solutions tend to merge toward the end of inflation. The dependence of $\dot{\phi}$ on the parameter n is relatively weak.

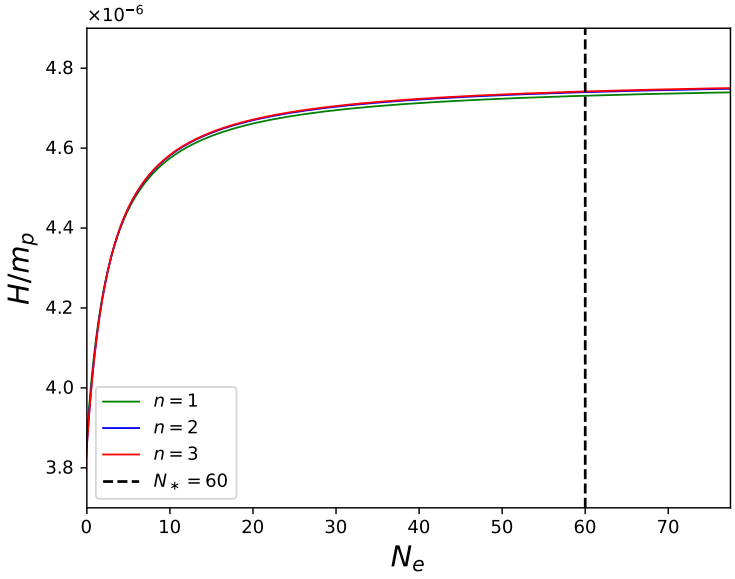

Figure 4.25: Time evolution of the Hubble parameter for the three T-models. The overall behaviour resembles that of $\dot{\phi}$, with different trajectories approximately equal to each other across the range of N_e.

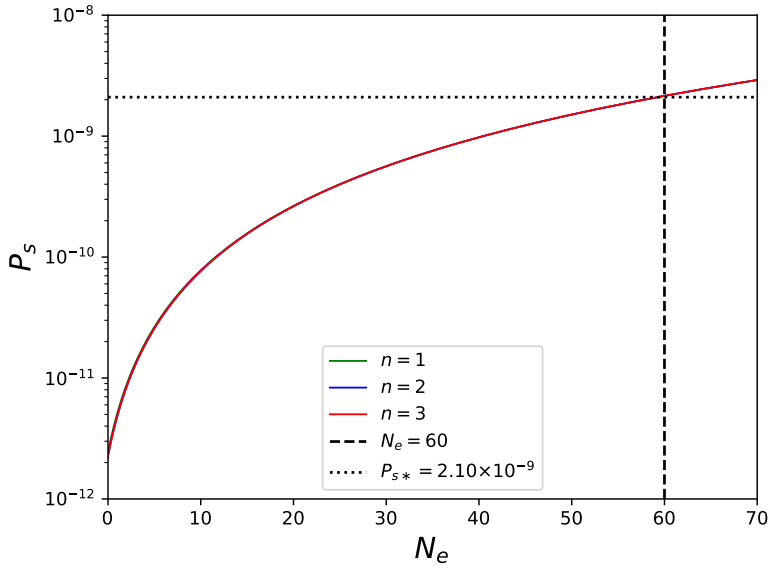

Figure 4.26: Scalar power spectrum P_S for modes crossing the Hubble radius at various N_e for $n = 1, 2, 3$ in the T-model potential. The three curves are nearly identical, and at the CMB pivot ($N_e = 60$), the values closely match the standard reference point.

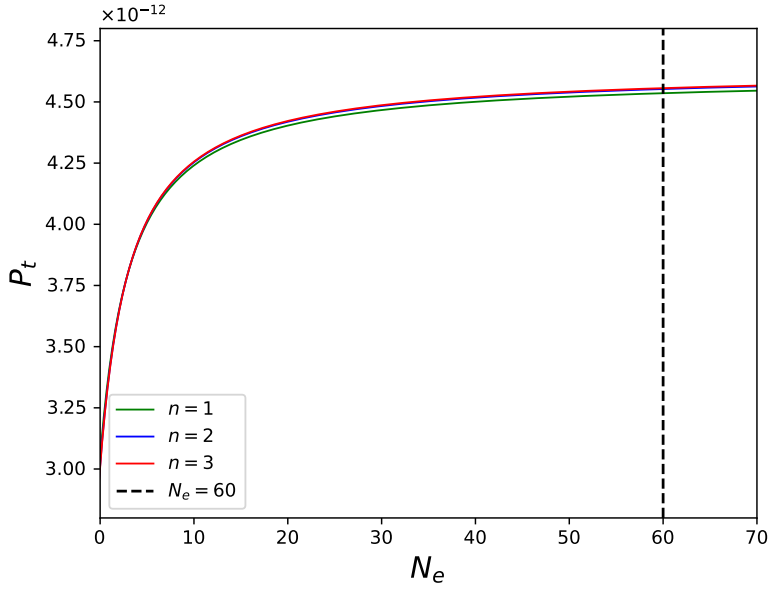

Figure 4.27: Tensor power spectrum P_T for different n-valued T-model potentials. Unlike P_S, the distinctions among the curves are slightly more noticeable, although their dependency on n is still pretty weak.

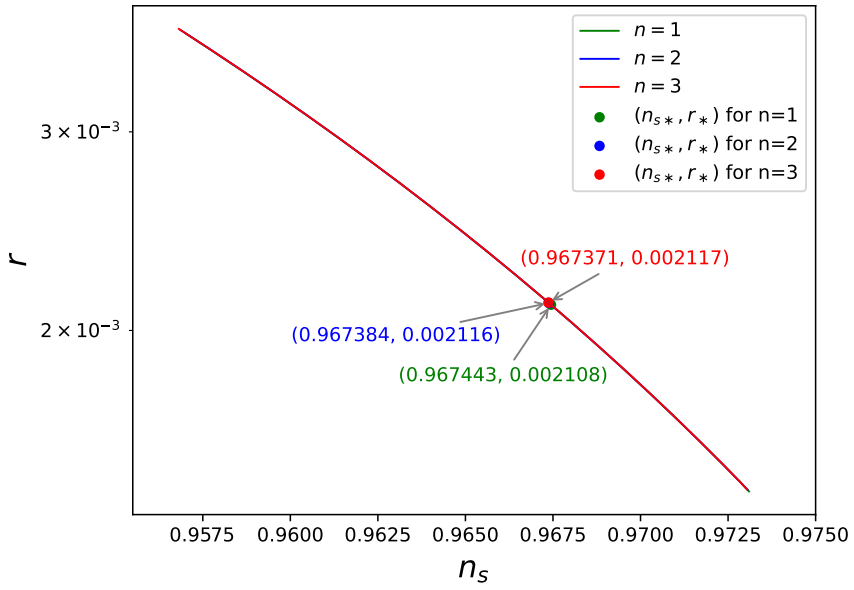

Figure 4.28: Tensor-to-scalar ratio r versus scalar spectral index n_S for three T-models of different n. The dependency of $n_S - r$ trajectory on n cannot be distinguished at all. At the CMB scale, r increases infinitesimally with n, though the values remain comfortably within the bound of (4.18).

Chapter 5

Conclusion and Future Works

In this report, we investigate the dynamics of inflationary models using both analytical tools and numerical methods, with particular emphasis on the evolution of perturbations across different inflationary potentials. By reformulating the equations of motion into a first-order dynamical system and employing robust numerical solvers, we were able to visualize and compare inflationary predictions for several representative models. These analyses revealed key qualitative features, such as slow-roll violation, attractor behavior, and the emergence of instabilities. Overall, the results highlight the value of careful numerical control in reliably extracting inflationary observables, such as the spectral index and tensor-to-scalar ratio.

The work presented here contributes to the study of inflation by proposing a unified workflow that integrates analytical understanding with flexible and transparent numerical experimentation. A distinctive aspect of this project is the development of a dedicated `Python` package designed to automate tasks such as defining inflationary potentials, computing effective masses, solving the dynamical system, and generating observable predictions. In contrast to existing numerical tools, this package aims to provide a modular and easily extensible framework suitable for exploring both standard and novel inflationary models. Although still under development, the framework represents a step toward lowering the technical barrier for new researchers in inflationary cosmology. Further refinement by supervisor guidance will be crucial to transforming it into a robust research environment.

Several directions offer promising opportunities for extending the present study. One natural step is to generalize the numerical framework to multi-field inflation, stochastic inflation, and models with non-canonical kinetic terms, thereby deepening comparison with the modern landscape of inflationary theory. Incorpo-

rating slow-roll reconstruction techniques or Bayesian parameter estimation would further allow these models to be confronted directly with observational datasets such as those from *Planck* or *BICEP/Keck*. Finally, the ongoing development of the `Python` automation package should continue with improved documentation, expanded functionality, and fine-tuning. With systematic refinement, the package can evolve into a powerful and user-friendly tool for exploring inflationary cosmology.

References

[1] N. Aghanim et al., "Planck 2018 results. I. Overview and the cosmological legacy of Planck," Astron. Astrophys., vol. 641, p. A1, 2020.

[2] B. Collaboration, "Improved constraints on primordial gravitational waves using planck, wmap, and bicep/keck observations through the 2018 season," Physical Review Letters, vol. 127, no. 15, p. 151301, 2021.

[3] A. H. Guth, "Inflationary universe: A possible solution to the horizon and flatness problems," Physical Review D, vol. 23, no. 2, pp. 347–356, 1981.

[4] A. D. Linde, "A new inflationary universe scenario: A possible solution of the horizon, flatness, homogeneity, isotropy and primordial monopole problems," Physics Letters B, vol. 108, no. 6, pp. 389–393, 1982.

[5] A. Albrecht and P. J. Steinhardt, "Cosmology for grand unified theories with radiatively induced symmetry breaking," Physical Review Letters, vol. 48, no. 17, pp. 1220–1223, 1982.

[6] R. Kallosh and A. Linde, "Universality class in conformal inflation," Journal of Cosmology and Astroparticle Physics, vol. 2013, no. 07, p. 002, 2013.

[7] A. Linde, "Single-field α-attractors," Journal of Cosmology and Astroparticle Physics, vol. 2015, no. 05, p. 003, 2015.

[8] A. A. Starobinsky, "A new type of isotropic cosmological models without singularity," Physics Letters B, vol. 91, pp. 99–102, 1980.

[9] V. Mukhanov, Physical Foundations of Cosmology. Cambridge University Press, 2005.

[10] S. Weinberg, Cosmology. Oxford University Press, 2008.

[11] B. Ryden, Introduction to Cosmology. Cambridge University Press, 2 ed., 2017.

[12] S. Dodelson, Modern Cosmology. Academic Press, 2003.

[13] D. Baumann, "Tasi lectures on inflation," arXiv preprint arXiv:0907.5424, 2009. TASI Lectures, University of Colorado, Boulder.

[14] S. Weinberg, Gravitation and Cosmology: Principles and Applications of the General Theory of Relativity. Wiley, 1972.

[15] N. Aghanim et al., "Planck 2018 results. VI. Cosmological parameters," Astron. Astrophys., vol. 641, p. A6, 2020. [Erratum: Astron.Astrophys. 652, C4 (2021)].

[16] D. Baumann, Cosmology. Cambridge University Press, 2022.

[17] D. Baumann, "Cosmology, part iii mathematical tripos." Lecture notes, 2025. Available online.

[18] A. R. Liddle and D. H. Lyth, Cosmological Inflation and Large-Scale Structure. Cambridge University Press, 2000.

[19] eBrary, "Problem horizon problem." `https://ebrary.net/202125/geography/problem_horion_problem`, 2025. Accessed: 2025-11-09.

[20] H. Ramírez, "Introduction to inflation — lecture notes." `https://www.uv.es/rarohec/inflation.html`, 2023. Accessed: 2025-11-10.

[21] D. Kazanas, "Dynamics of the universe and spontaneous symmetry breaking," Astrophysical Journal, vol. 241, pp. L59–L63, 1980.

[22] D. H. Lyth and A. Riotto, "Particle physics models of inflation and the cosmological density perturbation," Physics Reports, vol. 314, pp. 1–146, 1999.

[23] J. E. Lidsey, A. R. Liddle, E. W. Kolb, E. J. Copeland, T. Barreiro, and M. Abney, "Reconstructing the inflaton potential—an overview," Reviews of Modern Physics, vol. 69, pp. 373–410, 1997.

[24] E. W. Kolb and M. S. Turner, The Early Universe. Addison-Wesley, 1990.

[25] J. M. Bardeen, "Gauge-invariant cosmological perturbations," Phys. Rev. D, vol. 22, pp. 1882–1905, 1980.

[26] D. Wands, K. A. Malik, D. H. Lyth, and A. R. Liddle, "A new approach to cosmological perturbations," Phys. Rev. D, vol. 62, p. 043527, 2000.

[27] V. F. Mukhanov, "Gravitational instability of the universe filled with a scalar field," JETP Letters, vol. 41, pp. 493–496, 1985.

[28] L. P. Grishchuk, "Amplification of gravitational waves in an isotropic universe," Soviet Physics JETP, vol. 40, pp. 409–415, 1975.

[29] D. H. Lyth and A. R. Liddle, The Primordial Density Perturbation: Cosmology, Inflation and the Origin of Structure. Cambridge University Press, 2009.

[30] A. R. Liddle and S. M. Leach, "How long before the end of inflation were observable perturbations produced?," Physical Review D, vol. 68, p. 103503, 2003.

[31] Y. Akrami et al., "Planck 2018 results. X. Constraints on inflation," Astron. Astrophys., vol. 641, p. A10, 2020.

[32] M. Galante, R. Kallosh, A. Linde, and D. Roest, "Unity of cosmological inflation attractors," Physical Review Letters, vol. 114, no. 14, p. 141302, 2015.

[33] R. Kallosh and A. Linde, "Escher in the sky," Comptes Rendus Physique, vol. 16, no. 10, pp. 914–927, 2015.

[34] R. Kallosh and A. Linde, "On hilltop and brane inflation after planck," Journal of Cosmology and Astroparticle Physics, vol. 2019, p. 030, sep 2019.

[35] R. Kallosh and A. Linde, "Superconformal symmetry, supergravity and cosmology," Journal of High Energy Physics, vol. 2013, no. 06, pp. 1–25, 2013.

[36] S. Ferrara, R. Kallosh, A. Linde, and M. Porrati, "Superconformal symmetry, nmssm, and inflation," Physical Review D, vol. 88, no. 8, p. 085038, 2013.

[37] A. Linde, "α-attractors: Planck, lhc and dark energy," Journal of High Energy Physics, vol. 2015, no. 05, pp. 1–20, 2015.

[38] S. S. Bhatt, S. S. Mishra, S. Basak, and S. N. Sahoo, "Numerical simulations of inflationary dynamics: slow roll and beyond," 2024.

[39] P. Campeti and E. Komatsu, "New constraint on the tensor-to-scalar ratio from the planck and bicep/keck array data using the profile likelihood," The Astrophysical Journal, vol. 941, p. 110, dec 2022.

[40] S. S. Mishra and V. Sahni, "Canonical and non-canonical inflation in the light of the recent bicep/keck results," 2024.

Approval

The internship report titled **"Numerical analysis of inflationary α-attractor models"** submitted by **Masuk Ridwan Saumo**, a participant of the ICTP PWF: Physics for Bangladesh Online Summer Internship, has been found satisfactory in partial fulfillment of the requirements of the internship program.

The internship was conducted under the supervision of **Rafid Mahbub** during the period **15 July 2025** to **15 October 2025**.

Supervisor

Rafid Mahbub, Ph.D.

DataKind